琉球大学学術リポジトリ
University of the Ryukyus Repository

Title	Mesoscale Hybrid Data Assimilation System based on JMA Nonhydrostatic Model
Author(s)	Ito, Kosuke; Kunii, Masaru; Kawabata, Takuya; Saito, Kazuo; Aonashi, Kazumasa; Le, Duc
Citation	MONTHLY WEATHER REVIEW, 144: 3417-3439
Issue Date	2016-08-26
URL	http://hdl.handle.net/20.500.12000/37528
Rights	© 2016 American Meteorological Society

国立大学法人 琉球大学 University of the Ryukyus

Mesoscale Hybrid Data Assimilation System based on JMA Nonhydrostatic Model

KOSUKE ITO

University of the Ryukyus, Nishihara, and Meteorological Research Institute, Tsukuba, Japan

MASARU KUNII, TAKUYA KAWABATA, KAZUO SAITO, AND KAZUMASA AONASHI

Meteorological Research Institute, Tsukuba, Japan

LE DUC

Japan Agency for Marine-Earth Science and Technology, Yokohama, Japan

(Manuscript received 8 January 2016, in final form 6 June 2016)

ABSTRACT

This paper discusses the benefits of using a hybrid ensemble Kalman filter and four-dimensional variational (4D-Var) data assimilation (DA) system rather than a 4D-Var system employing the National Meteorological Center (NMC, now known as NCEP) method (4D-Var-Bnmc) to predict severe weather events. An adjoint-based 4D-Var system was employed with a background error covariance matrix **B** constructed from the NMC method and perturbations in a local ensemble transform Kalman filter system. The DA systems are based on the Japan Meteorological Agency's nonhydrostatic model. To reduce the sampling noise, three types of implementation (the spatial localization, spectral localization, and neighboring ensemble approaches) were tested. The assimilation of a pseudosingle observation of sea level pressure located at a tropical cyclone (TC) center yielded analysis increments physically consistent with what is expected of a mature TC in the hybrid systems at the beginning of the assimilation window, whereas analogous experiments performed using the 4D-Var-Bnmc system did not. At the end, the structures of the 4D-Var-based increments became similar to one another, while the analysis increment by the 4D-Var-Bnmc system was broad in the horizontal direction. Realistic DA experiments showed that all of the hybrid systems provided initial conditions that yielded more accurate TC track and intensity forecasts than those achievable by the 4D-Var-Bnmc system. The hybrid systems also yielded some statistically significant improvements in forecasting local heavy rainfall events in terms of fraction skill scores when a 160 km × 160 km window size was used. The overall skills of the hybrid systems were relatively independent of the choice of implementation.

1. Introduction

The prediction of high-impact weather events is of particular importance in the field of atmospheric sciences. Recent efforts have substantially improved the ability to forecast such events (Courtier et al. 1994; Hunt et al. 2004; Kunii 2014; Saito 2012). To realize further improvements, a more sophisticated data assimilation (DA) method that provides better initial conditions suitable for high-impact weather is required, as are further developments in the physics of the numerical models.

The Japan Meteorological Agency (JMA) has incorporated an adjoint-based four-dimensional variational (4D-Var) DA method into their regional forecast system, which is based on the JMA nonhydrostatic model [JMA-NHM; for details, see Saito et al. (2006)]. The JMA-NHM-based variational DA (JNoVA; Honda and Sawada 2009; Honda et al. 2005) system has been used operationally by the JMA to perform mesoscale analysis for regional forecasts since 7 April 2009.

Denotes Open Access content.

Corresponding author address: Kosuke Ito, Department of Physics and Earth Sciences, University of the Ryukyus. 1 Sembaru, Nishihara, Okinawa 903-0213, Japan.
E-mail: itokosk@sci.u-ryukyu.ac.jp

DOI: 10.1175/MWR-D-16-0014.1

© 2016 American Meteorological Society

The JNoVA system has substantially improved the accuracy of severe rainfall event forecasts compared with those of the hydrostatic-model-based 4D-Var method (Honda et al. 2005). To further enhance the forecast quality, the modeling of the background error covariance **B** used for the JNoVA system should be more sophisticated because at the beginning of the 4D-Var assimilation window the specified **B** governs the structure of the analysis increment in addition to the innovation and model dynamics (Johnson et al. 2005). Therefore, improved specification of this prescribed matrix will contribute to more accurate modeling of the developing modes that are related to high-impact weather.

Traditionally, **B** has been assumed to be static over time in the JNoVA system, according to the National Meteorological Center (NMC, now known as NCEP) method, which uses the differences between a series of two forecasts that are valid at the same time (Parrish and Derber 1992). Although **B**, as obtained from the NMC method, approximates the climatological background error covariance, recent studies have shown that the forecast quality made by the 4D-Var system can be enhanced further by making **B** flow-dependent based on the perturbations evolved in an ensemble Kalman filter (EnKF) system, which is a hybrid DA system (Bonavita et al. 2012; Buehner et al. 2010a,b; Lorenc 2003a; Wang et al. 2007).

Several operational centers employ hybrid DA systems for their global-scale forecasts (Bonavita et al. 2012; Clayton et al. 2013; Kleist and Ide 2015; Kuhl et al. 2013). However, the benefits of using a hybrid system can be more pronounced in severe weather event predictions because climatological estimates do not reflect the flow-dependent nature of background error covariances for high-impact and quickly evolving phenomena. Recently, 3D-Var DA experiments using ensemble-based **B** were developed, and the abilities of the developed systems to forecast tropical cyclones (TCs) and local heavy rainfall events were tested (Pan et al. 2014; Schwartz and Liu 2014; Schwartz et al. 2013). Only a few studies have focused on mesoscale weather prediction using hybrid EnKF-4D-Var systems (Poterjoy and Zhang 2014; Zhang and Zhang 2012). Therefore, further experiments are needed to confirm the benefits by analyzing large numbers of samples.

The main objective of this study was to determine whether the use of an ensemble-based **B** could enhance the accuracy of severe weather predictions initialized by a DA system almost identical to the JMA operational mesoscale 4D-Var system. To do so, we computed **B** by using a local ensemble transform Kalman filter DA system (LETKF; Hunt et al. 2007), which is based on the JMA-NHM (Kunii 2014), and performed 62 forecasts of four intense TCs and 104 forecasts of three local heavy rainfall events that occurred in 2011–12. The results will contribute to the design of future DA systems and will facilitate the prevention and mitigation of weather-related disasters.

The remainder of this paper is organized as follows. Section 2 describes the mathematical background and DA systems. In section 3, the results of the single-observation experiment are presented. In sections 4 and 5, the forecast quality of the hybrid system is evaluated for the four strongest TCs and three local heavy rainfall events, respectively. Finally, our conclusions are summarized in section 6.

2. Methodology

a. Formulation of mesoscale hybrid system

Among the many options for implementing flow-dependent ensemble covariances in 4D-Var DA systems (Buehner 2005; Lorenc 2003a; Wang et al. 2007), we chose to develop an adjoint-based 4D-Var system using a mixture of NMC-based and flow-dependent background error covariances. A flow-dependent **B** is constructed from perturbations in the EnKF. The analysis field obtained from the hybrid system is not used to update subsequent EnKF cycles, unlike in the ''two-way'' hybrid system of Poterjoy and Zhang (2014).

The 4D-Var DA system used in JNoVA employs the incremental approach following remark 5 in section 3 of Courtier et al. (1994). A high-resolution model is first run to calculate the innovation vector (observation minus high-resolution background state projected into observation space). At each iteration, a simplified nonlinear version of the JMA-NHM is used to provide trajectories with coarse resolution. The adjoint model, which is based on the tangent linear model corresponding to the simplified nonlinear model, is used to calculate the gradient of the cost function. A low-resolution analysis increment at the beginning of the assimilation window is obtained as a result of the minimization procedure. By running a high-resolution model with this analysis increment interpolated to a fine mesh, a high-resolution analysis increment is obtained at the end of assimilation window (Courtier et al. 1994; JMA 2013, section 2.6.3).

The cost function used in this study is defined as

$$J(\delta\mathbf{x}_0) = \frac{1}{2}\delta\mathbf{x}_0^{\mathrm{T}}\mathbf{B}^{-1}\delta\mathbf{x}_0 + \frac{1}{2}\sum_t \{\mathbf{d}_t + H_t[M_t(\mathbf{x}_b)] - H_t[M_t(\delta\mathbf{x}_0 + \mathbf{x}_b)]\}^{\mathrm{T}}\mathbf{R}_t^{-1}\{\mathbf{d}_t + H_t[M_t(\mathbf{x}_b)] - H_t[M_t(\delta\mathbf{x}_0 + \mathbf{x}_b)]\} + J_p, \quad (1)$$

where $\delta\mathbf{x}_0$ is the analysis increment of the initial state vector $\mathbf{x}_0$ with respect to the first guess initial state vector $\mathbf{x}_b$, which is defined at low-resolution model grid points; $\mathbf{R}$ is the observation error covariance matrix; H is the nonlinear observation operator that projects low-resolution model variables onto the observation space; and M is the simplified nonlinear model integration operator from the initial time. The innovation vector $\mathbf{d}$ is given by $\mathbf{d} = \mathbf{y} - \hat{H}(\hat{\mathbf{x}}_b)$, where $\mathbf{y}$ is an observation vector, $\hat{H}$ is the observation operator projecting the high-resolution model variables onto the observation space, and $\hat{\mathbf{x}}$ is the state vector defined at high-resolution grid points. The superscript T represents the transpose, and the subscripts 0 and t represent the values at times 0 and t, respectively. The J_p term is a penalty term that is included to suppress spurious inertia–gravity waves (Honda et al. 2005).

Note that the current J is different from the cost function employed in several operational centers according to remark 4 in section 3 of Courtier et al. (1994), which is also known as an incremental approach:

$$J(\delta\mathbf{x}_0) = \frac{1}{2}\delta\mathbf{x}_0^{\mathrm{T}}\mathbf{B}^{-1}\delta\mathbf{x}_0 + \frac{1}{2}\sum_t(\mathbf{d}_t - \mathbf{H}_t\mathbf{M}_t\delta\mathbf{x}_0)^{\mathrm{T}}\mathbf{R}_t^{-1}(\mathbf{d}_t - \mathbf{H}_t\mathbf{M}_t\delta\mathbf{x}_0) + J_p, \tag{2}$$

where $\mathbf{H}_t$ is a linearized low-resolution observation operator and $\mathbf{M}_t$ is a low-resolution tangent linear model operator from time 0 to t. This cost function can be made equivalent to the current cost function [Eq. (1)] by using a first-order Taylor series $H_t[M_t(\delta\mathbf{x}_0 + \mathbf{x}_b)] = H_t[M_t(\mathbf{x}_b)] + \mathbf{H}_t\mathbf{M}_t\delta\mathbf{x}_0$, which holds true reasonably well in JNoVA (Honda 2010).

In the current work, a perturbed run with the simple nonlinear model instead of the tangent linear model was conducted in JNoVA to obtain the cost function and its gradient. Because the simplified nonlinear model is cheaper than the tangent linear model, this implementation method reduces the calculation time.

Our hybrid system uses a background error covariance $\mathbf{B}_{\mathrm{hyb}}$ given by a weighted sum of an NMC-based covariance matrix $\mathbf{B}_{\mathrm{NMC}}$ and an ensemble-based covariance matrix $\mathbf{B}_{\mathrm{ens}}$ (Hamill and Snyder 2000):

$$\mathbf{B}_{\mathrm{hyb}} = \beta\mathbf{B}_{\mathrm{NMC}} + (1-\beta)\mathbf{B}_{\mathrm{ens}}, \tag{3}$$

where β is a scalar weight, which was set to 0.2 as in the default experiment by Zhang and Zhang (2012). The analysis increment by the hybrid system $\delta\mathbf{x}_0$ can be expressed in terms of the contributions of the two covariances as follows:

$$\delta\mathbf{x}_0 = \sqrt{\beta}\delta\mathbf{x}_{\mathrm{NMC}} + \sqrt{1-\beta}\delta\mathbf{x}_{\mathrm{ens}}. \tag{4}$$

The ratio of $\sqrt{\beta}$ to $\sqrt{1-\beta}$ is 1:2 (0.447 and 0.894).

The cost function [Eq. (1)] can be rewritten in terms of new control variables $\delta\mathbf{v}_{\mathrm{NMC}}$ and $\delta\mathbf{v}_{\mathrm{ens}}$, which are defined as

$$\delta\mathbf{x}_{\mathrm{NMC}} = \mathbf{B}_{\mathrm{NMC}}^{1/2}\delta\mathbf{v}_{\mathrm{NMC}} \tag{5}$$

and

$$\delta\mathbf{x}_{\mathrm{ens}} = \mathbf{B}_{\mathrm{ens}}^{1/2}\delta\mathbf{v}_{\mathrm{ens}}. \tag{6}$$

Substituting Eqs. (5) and (6) into Eq. (1), a new form of the cost function can be obtained:

$$J = \frac{1}{2}\delta\mathbf{v}_{\mathrm{NMC}}^{\mathrm{T}}\delta\mathbf{v}_{\mathrm{NMC}} + \frac{1}{2}\delta\mathbf{v}_{\mathrm{ens}}^{\mathrm{T}}\delta\mathbf{v}_{\mathrm{ens}} + \frac{1}{2}\sum_t\{\mathbf{d}_t + H_t[M_t(\mathbf{x}_b)] - H_t[M_t(\delta\mathbf{x}_0 + \mathbf{x}_b)]\}^{\mathrm{T}}\mathbf{R}_t^{-1}\{\mathbf{d}_t + H_t[M_t(\mathbf{x}_b)] - H_t[M_t(\delta\mathbf{x}_0 + \mathbf{x}_b)]\} + J_p. \tag{7}$$

The gradients of the cost function J with respect to $\delta\mathbf{v}_{\mathrm{NMC}}$ and $\delta\mathbf{v}_{\mathrm{ens}}$ are

$$\frac{\partial J}{\partial\delta\mathbf{v}_{\mathrm{NMC}}} = \delta\mathbf{v}_{\mathrm{NMC}} - \sqrt{\beta}\mathbf{B}_{\mathrm{NMC}}^{1/2}\sum_t\mathbf{M}_t^{\mathrm{T}}\mathbf{H}_t^{\mathrm{T}}\mathbf{R}_t^{-1}\{\mathbf{d}_t + H_t[M_t(\mathbf{x}_b)] - H_t[M_t(\delta\mathbf{x}_0 + \mathbf{x}_b)]\} + \frac{\partial J_p}{\partial\delta\mathbf{v}_{\mathrm{NMC}}} \tag{8}$$

and

$$\frac{\partial J}{\partial\delta\mathbf{v}_{\mathrm{ens}}} = \delta\mathbf{v}_{\mathrm{ens}} - \sqrt{1-\beta}\mathbf{B}_{\mathrm{ens}}^{1/2}\sum_t\mathbf{M}_t^{\mathrm{T}}\mathbf{H}_t^{\mathrm{T}}\mathbf{R}_t^{-1}\{\mathbf{d}_t + H_t[M_t(\mathbf{x}_b)] - H_t[M_t(\delta\mathbf{x}_0 + \mathbf{x}_b)]\} + \frac{\partial J_p}{\partial\delta\mathbf{v}_{\mathrm{ens}}}. \tag{9}$$

The set of Eqs. (3)–(9) defines an optimization problem that can be solved by using the limited-memory quasi-Newton algorithm (Liu and Nocedal 1989) and the adjoint model operator $\mathbf{M}_t^{\mathrm{T}}$.

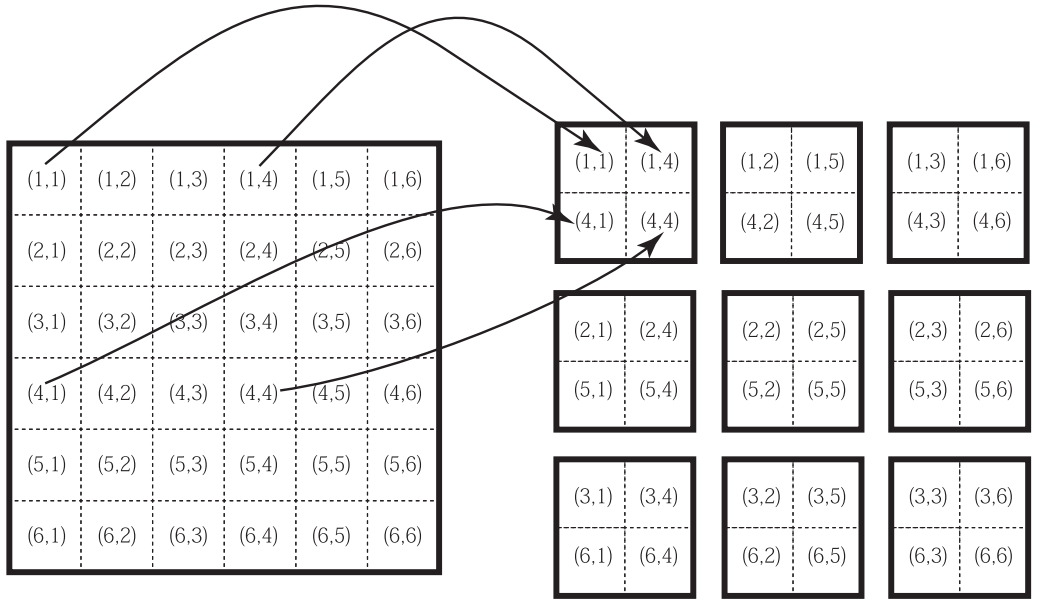

FIG. 1. Schematic illustration of an example of a neighboring ensemble approach. Original single realization defined in 15-km mesh is regarded as nine different realizations forming 45-km mesh.

b. *Modeling of background error covariances*

Suppose that perturbations are obtained from an EnKF system, and let $\mathbf{X} = (\mathbf{x}_1, \mathbf{x}_2, \ldots, \mathbf{x}_N)$ be the deviation with respect to the ensemble mean normalized by $\sqrt{N-1}$, where N is the ensemble size. When special treatments are not applied, the "raw" sample ensemble covariance and square root matrix are (Wang et al. 2007)

$$\mathbf{B}_{\text{ens}} = \mathbf{X}\mathbf{X}^{\mathrm{T}} \tag{10}$$

and

$$\mathbf{B}_{\text{ens}}^{1/2} = \mathbf{X}. \tag{11}$$

In this case, the size of $\mathbf{B}_{\text{ens}}^{1/2}$ is $K \times N$, where K represents the dimension of the state vector, and the dimension of $\delta\mathbf{v}_{\text{ens}}$ is N.

This raw background error covariance matrix [Eq. (10)] includes the sampling errors resulting from the lack of ensemble members in a large-dimensional system. To remedy this problem, three types of modeling are tested in current hybrid DA systems. One is a spatial localization approach, which involves replacing Eq. (10) by

$$\mathbf{B}_{\text{ens}} = (\mathbf{X}\mathbf{X}^{\mathrm{T}}) \circ \mathbf{C}, \tag{12}$$

where $\mathbf{C}$ is a correlation matrix describing a function that becomes zero over some prescribed distance between two analysis grid points, r_a, and the operator $\circ$ represents a Schur product. This approach has been used to suppress spurious sampling noise in many previous studies (Buehner et al. 2010a,b; Clayton et al. 2013; Lorenc 2003b; Zhang and Zhang 2012). To implement this $\mathbf{B}_{\text{ens}}$, the so-called alpha control vector $\boldsymbol{\alpha}_{\text{ens}}$, which has a length of NK', where K' represents the rank of $\mathbf{C}$, is defined by $\delta\mathbf{x}_{\text{ens}} = \mathbf{B}_{\text{ens}}^{1/2}\boldsymbol{\alpha}_{\text{ens}}$, as in Eq. (6). The formulation of $\mathbf{B}_{\text{ens}}^{1/2}$ and $\boldsymbol{\alpha}_{\text{ens}}$ is the same as in Eqs. (A1) and (A2) of Wang et al. (2007). This method currently requires substantial computational resources since the control vector is quite long, although Bishop et al. (2011) proposed an efficient localization approach. Hereafter, a hybrid DA system that uses Eq. (12) is referred to as the 4D-Var-BenkfL system.

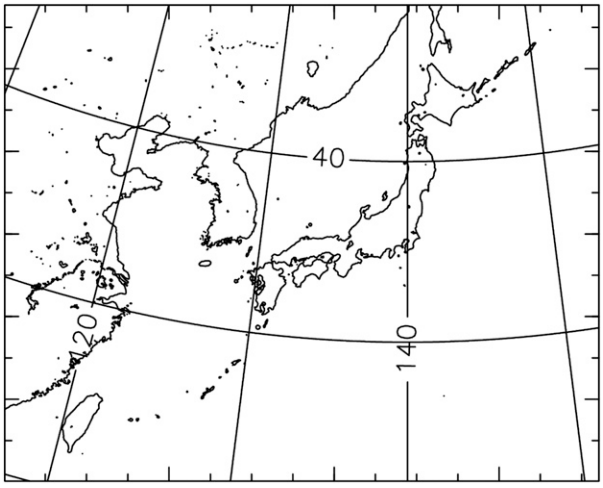

FIG. 2. Calculation domain.

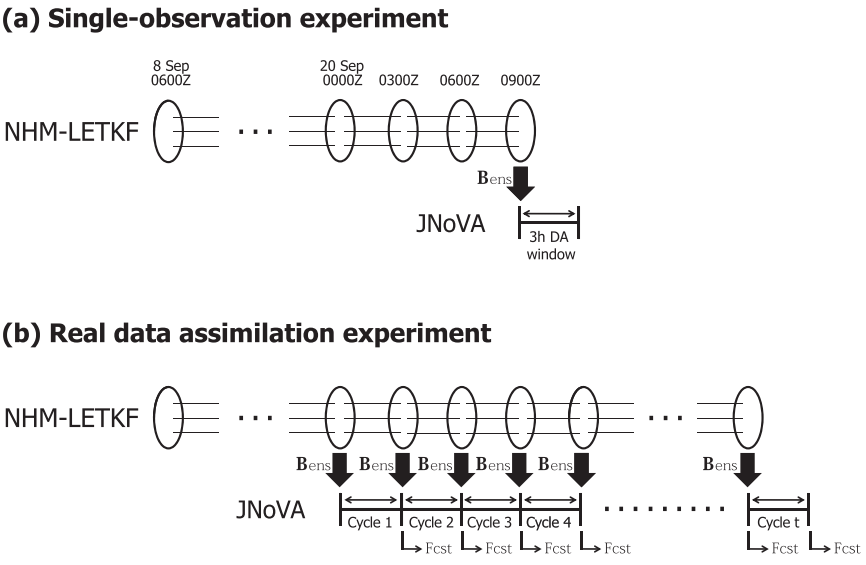

FIG. 3. Time scheduling of DA cycles in hybrid systems.

The second approach is to construct $\mathbf{B}_{\rm ens}^{1/2}$ based on spectral localization. This approach relies on the hypothesis that the amplitude of the correlations in spectral space generally decreases as the absolute difference between the wavenumbers of pairs of spectral components increases (Buehner and Charron 2007). Spectral localization has been shown to reduce analysis error systematically by eliminating the rapid spatial variations, while it is not effective at removing spurious correlations between variables at distant grid points. Buehner and Charron (2007) showed that spectral localization in spectral space can be equivalent to spatial smoothing of the correlation functions in gridpoint space. In a discretized form, an element of a spectrally localized background error covariance matrix for a variable at points i and j becomes (for simplicity, the expression is shown for one-dimensional case):

$$\begin{aligned} B(i,j) &= \sigma(i)\sigma(j)C_{sl}(i,j) \\ &= \sigma(i)\sigma(j)\Delta s \sum_{n=1}^{N}\sum_{m\in\mathbb{Z}} e_n(i+m\Delta s)e_n(j+m\Delta s)L(m\Delta s), \end{aligned} \tag{13}$$

where $\sigma(i)$ is a standard deviation at point i; $C_{sl}(i,j)$ is the spectrally localized correlation in gridpoint space; $m\Delta s$ is the spatial shift for integer m; $e_n(i')$ is an element of $\delta\mathbf{x}_n$, where n is an index of ensemble member, at location i'; and $L(m\Delta s)$ is the inverse transform of spectral localization weight satisfying

$$\Delta s \sum_{m\in\mathbb{Z}} L(m\Delta s) = 1. \tag{14}$$

From Eq. (13), an element of the square root matrix can be written as

$$B^{1/2}(i,k_{n,m}) = \sigma(i)e_n(i+m\Delta s)\sqrt{L(m\Delta s)\Delta s}, \tag{15}$$

where the index k runs over all members and spatial shifts. The shifted ensemble members can simply be considered as a much larger ensemble N', which equals N multiplied by the total number of shifted grid points. In this case, the size of $\mathbf{B}_{\rm ens}^{1/2}$ is $K \times N'$, and the dimension of $\delta\mathbf{x}_{\rm ens}$ is N'. Excluding the cost to obtain EnKF results, the additional computational cost for incorporating a spectrally localized $\mathbf{B}$ is smaller than the cost required for the 4D-Var-BenkfL system because the additional length of the control vector is just N'. Hereafter, a hybrid DA system that employs the spectral localization approach is referred to as a 4D-Var-BenkfS system.

The calculation cost can be further decreased by generating an analysis field only at the target grid point that is coarsely defined at a grid spacing of $m'\Delta s$ for a constant integer m' (which was set to 3 in the current work) and by assuming $L = 0$ in Eq. (13) outside a neighboring block centered at the target grid point (Aonashi et al. 2013; Aonashi et al. 2015, manuscript submitted to *Mon. Wea. Rev.*). This approach is schematically illustrated in Fig. 1. As shown, the number of pseudoensemble members is Nm'^2. The additional length of the control vector is just Nm'^2, and the size of $\mathbf{B}_{\rm ens}^{1/2}$ becomes $(K/m'^2) \times (m'^2N)$. After obtaining the analysis increments at the coarse grid points, they are interpolated into the original analysis field grid points to continue the iterations in the 4D-Var minimization

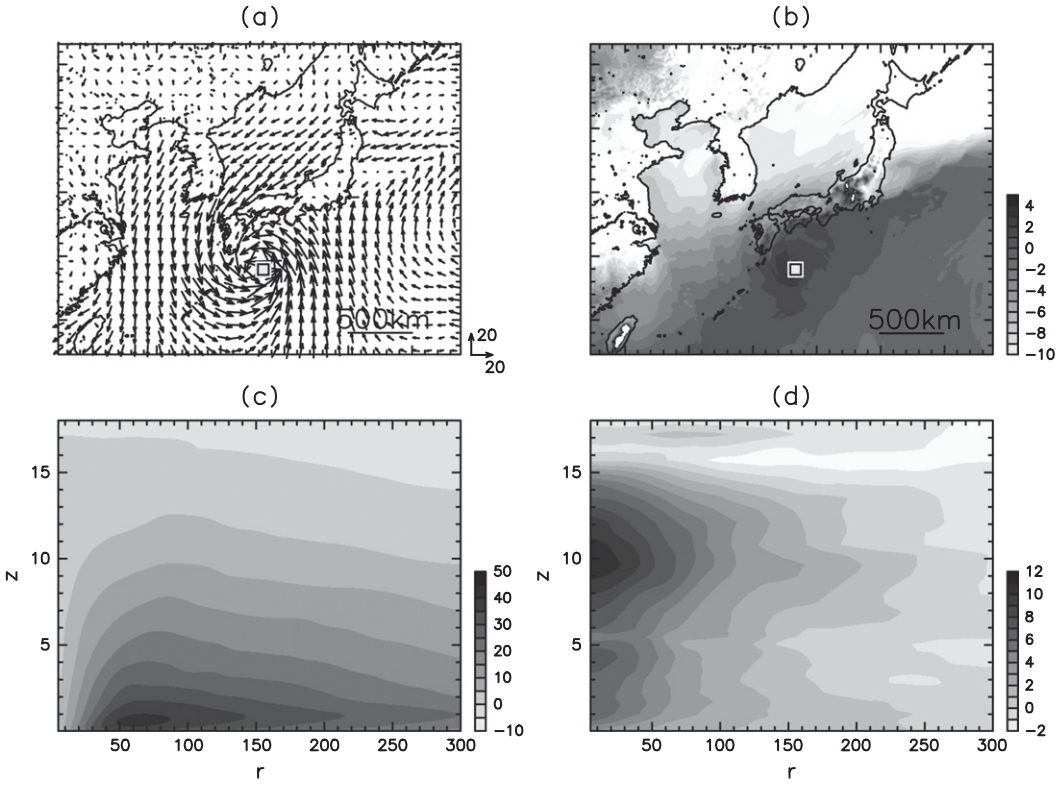

FIG. 4. First guesses of (a) horizontal wind ($m\,s^{-1}$) at ninth level (z_h = 0.68 km); (b) potential temperature anomaly (K) relative to basic state at 33rd level (z_h = 9.63 km); (c) azimuthal mean of tangential velocity ($m\,s^{-1}$) centered at TC, where horizontal coordinate r and vertical coordinate z_h indicate distance from TC center and height in hybrid coordinates (km), respectively; and (d) azimuthal mean of potential temperature deviation (K) from area-averaged potential temperature within $r < 1000$ km. Unit vector and shading scales are shown to the right of each panel.

process. Hereafter, this technique is referred to as the neighboring ensemble approach, and we call a hybrid DA system that employs this approach a 4D-Var-BenkfN system.

c. *JNoVA*

The framework of JNoVA is outlined in this subsection. More detailed explanations are given in Honda and Sawada (2009) and JMA (2013). The high-resolution forward model with 5 km horizontal grid spacing employs a horizontally explicit and vertically implicit scheme as a dynamical core with six-category bulk microphysics (Ikawa and Saito 1991), the modified Kain–Fritsch convective scheme (Kain and Fritsch 1990), and a radiation scheme. Boundary layer turbulence is determined by the Mellor–Yamada–Nakanishi–Niino level-3 closure model (Nakanishi and Niino 2004).

The physical processes retained in our adjoint and simplified nonlinear models with 15-km horizontal grid spacing are similar to those in the forward model, although they include several simplifications such as the replacement of the convective scheme with large-scale condensation and moist convective adjustment. The length of the assimilation window is 3 h. The observed data were divided into the following four time slots within each 3-h assimilation window: 0.0–0.5, 0.5–1.5, 1.5–2.5, and 2.5–3.0 h. The standard deviation of the observation error is described in section 2.6.4 of JMA (2013).

d. *LETKF*

The ensemble-based background error covariance in our hybrid system uses perturbations in the LETKF system based on JMA-NHM (Kunii 2014). The embedded dynamical model is similar to that in the simplified nonlinear model of the JNoVA system. Currently, this LETKF system operates with 15-km grid spacing and employs four-dimensional LETKF (Hunt et al. 2004). The observed data were divided into the following three time slots within each 3-h assimilation window: 0.5–1.5, 1.5–2.5, and 2.5–3.5 h; thus, this LETKF system uses a slightly different

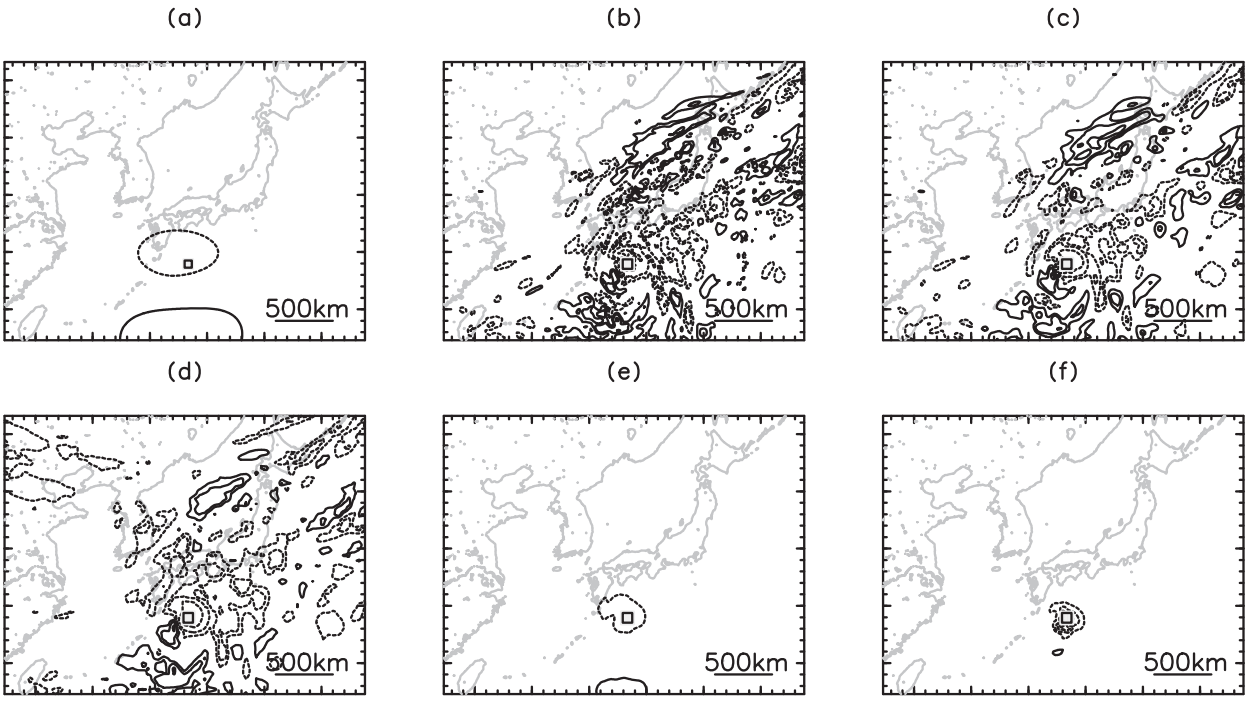

FIG. 5. Analysis increment of potential temperature at 33rd vertical level (approximately 9.63 km) at $t = 0$ h by (a) 4D-Var-Bnmc, (b) 4D-Var-Benkf0, (c) 4D-Var-BenkfS, (d) 4D-Var-BenkfN, and (e) 4D-Var-BenkfL systems. (f) As in (e), but for ensemble-based part of analysis increment [$\sqrt{1-\beta}\delta\mathbf{x}_{\rm ens}$ in Eq. (3)]. Contours are drawn at ±0.05, ±0.1, ±0.2, ±0.4, ±0.8, and ±1.6 K in (a)–(e). Solid lines indicate positive values, while dotted lines indicate negative values. For (f), contour interval (CI) is set to constant value of 0.01 K. Zero contours have been omitted. Rectangles indicate location at which sea level pressure observation was added at $t = 3$ h.

partitioning scheme from JNoVA. The spatial localization depends on the physical distance between an analysis grid point and an observation location r_o, which is known as observation localization, rather than r_a.

e. Assimilated data

The data used in the realistic DA experiments were conventional observations recorded by surface stations, radiosondes, ships, aircraft, and vertically integrated precipitable water measurements derived from ground-based global positioning systems, wind profiles, Doppler radar radial velocity data, and TC bogus data [see JMA (2013) for details]. These data had already been subjected to several quality control checks in the operational system at the JMA. Note that although the JMA operational DA system assimilates satellite radiance and radar/rain gauge-analyzed precipitation (RAP; Nagata 2011), they are not assimilated in the current work because the LETKF system has not yet implemented the observation operator.

f. Configurations

The background error covariance in the original JNoVA system was constructed according to the NMC method using the statistics of pairs of 12- and 6-h forecasts made between January and December 2005. Hereafter, a 4D-Var system that uses only $\mathbf{B}_{\rm NMC}$ is called a 4D-Var-Bnmc system. In the hybrid DA systems, LETKF- and NMC-based background error covariances are combined [Eq. (3)].

The calculation domain is identical to that used in JMA operational regional forecasts as of 2012. Its 3600 km × 2880 km area encompasses Japan and the surrounding regions[1] (Fig. 2). The domain is discretized into 721 × 577 grid points with 5-km grid spacing in the forecast model and the high-resolution model of the JNoVA system, while it is discretized into 241 × 193 grid points with 15-km grid spacing in the LETKF system and the simplified nonlinear model of the JNoVA system. The LETKF system and the high-resolution model of the JNoVA system contain 50 vertical levels in the hybrid[2] terrain following coordinate z_h (Ishida 2007),

[1] In March 2013, the domain in the JMA operational regional forecast was extended to 4080 km × 3300 km (see http://www.jma.go.jp/jma/jma-eng/jma-center/nwp/specifications_models.pdf).

[2] Here, "hybrid" means the combination of the z^* coordinate near the surface and the z coordinate near the top of the model, which is not the same as its meaning in relation to the 4D-Var and EnKF systems.

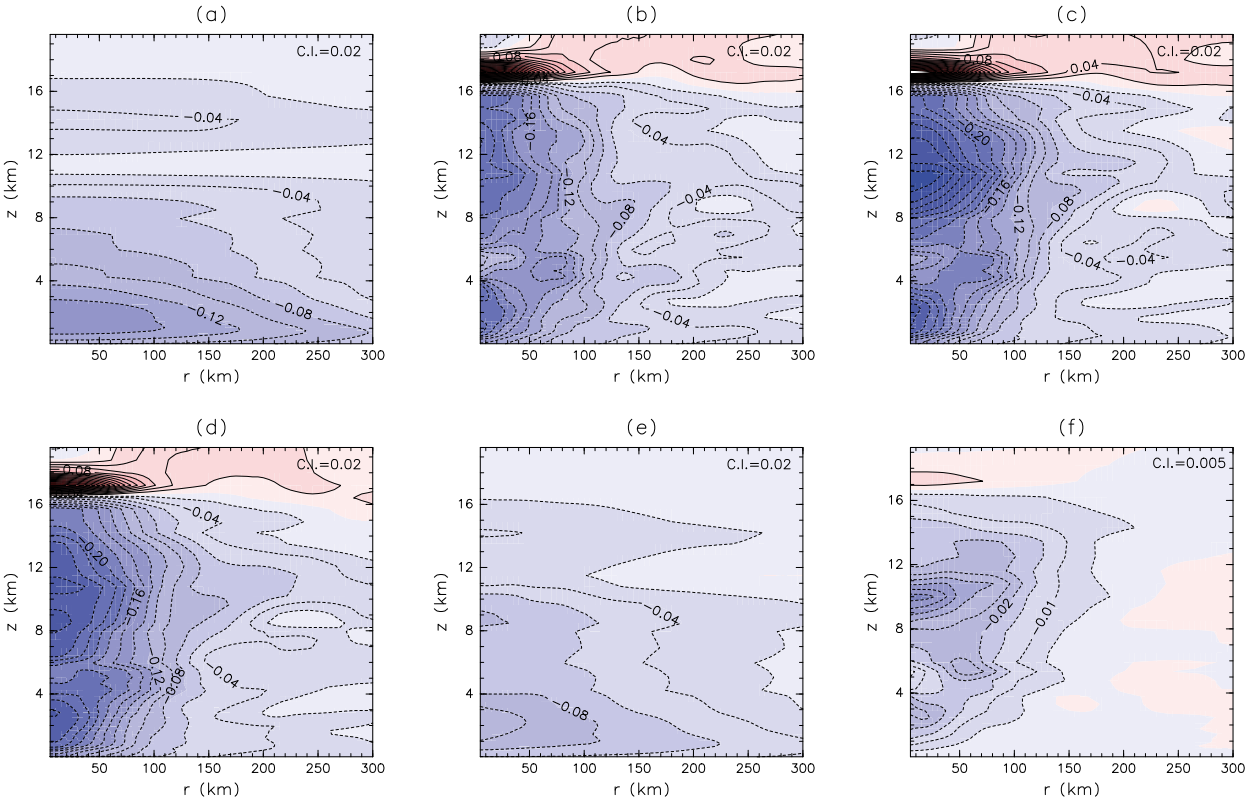

FIG. 6. As in Fig. 5, but for analysis increment of azimuthally averaged potential temperature (K) at $t = 0$ h. CI is shown in the upper right of each panel, and zero contours have been omitted. Note that (f) employs a different contour interval from the other panels.

while the simplified nonlinear model of the JNoVA system contains 40 vertical levels. The model top is around 22 km. See section 2.7 of Honda (2010) for more details about the vertical grid spacings.

A total of 50 ensemble members is used in the LETKF system. The localization factor depends on r_o. The fifth-order polynomial of Eq. (4.10) of Gaspari and Cohn (1999), which approximates a Gaussian function, is used as the covariance localization function. The spatial localization scale (corresponding to the one-sigma length at which the approximated Gaussian localization function became $e^{-0.5}$ in this study) is 200 km in the horizontal direction and $0.2 \ln p$ in the vertical direction, as in Kunii (2014). For the 4D-Var-BenkfL system, the localization scale is 200 km in the horizontal direction, and model levels in z_h coordinates that are equivalent to $0.2 \ln p$ of the basic field make the localization scale similar to that used in LETKF. For the 4D-Var-BenkfS system, the same fifth-order polynomial as in 4D-Var-BenkfL is used to define a function of $L(m\Delta s)$ for "localizing" the horizontal covariance in gridpoint space. The localization scale is 15 km. In the 4D-Var-BenkfN system, the value of $L(m\Delta s)$ is simply set to the same weight within a block of 3×3 grid points centered at a target point and 0 outside the block.

The lateral boundary conditions in the forecast were provided every hour by the JMA operational global spectral model with TL959. They are not modified in any of the systems using the DA technique, although they are perturbed to prevent underdispersive spread in the LETKF system (Saito et al. 2012). The lateral boundary perturbations in the LETKF system were derived from the JMA operational 1-week ensemble prediction system that is based on the global spectral model with TL319 after subtracting the ensemble mean state (Kunii 2014; Saito et al. 2010).

For the single-observation experiment described in section 3, we compared the analysis increments derived from the 4D-Var-Bnmc and hybrid DA systems. We also performed an experiment in which the background error covariances were constructed from the raw perturbations by employing Eq. (10) to demonstrate the impact of the localization and neighboring ensemble approach that is referred to as the 4D-Var-Benkf0 system.

For the realistic DA experiments, we conducted the analysis by using the DA systems. The spinup time of the LETKF cycles was more than one week. For TC detection, we followed the same procedure as Ito et al.

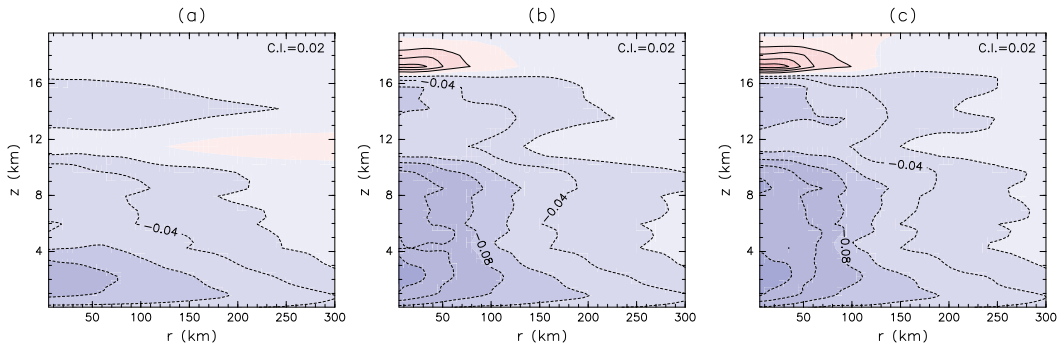

FIG. 7. As in Fig. 6, but for analysis increment in (a) EXP_h2, (b) EXP_novert, and (c) EXP_h2novert.

(2015). After completing each realistic DA experiment with a time interval of 3 h, we conducted 36-h deterministic forecasts to evaluate the quality of each DA system. These runs were initialized by the analysis state at the end of the assimilation window for the 4D-Var-based systems. The time scheduling is summarized for the hybrid DA systems in Fig. 3. Although our main objective was to verify the improvements over the 4D-Var-Bnmc system that resulted from using these hybrid DA systems, we also performed forecasts starting from an ensemble mean analysis state in the LETKF system for reference.

To judge the statistical significance of the improvements made by the LETKF and the hybrid systems with respect to the 4D-Var-Bnmc system, a two-tailed t test for two paired samples was applied. Although we obtained the samples from forecast experiments initialized eight times a day, the sample size was replaced by the effective sampling size in order to account for the persistence of the sequential time data according to Kuhl et al. (2013).

3. Single-observation experiment

To check the correct implementation of our system before the realistic DA experiment, we conducted a single-observation assimilation experiment. The 3-h DA window lasted from 0900 until 1200 UTC 20 September 2011 (in this discussion, the beginning and end of the 3-h assimilation window are referred to as $t = 0$ and $t = 3$ h, respectively). We introduced a minimum sea level pressure (MSLP) innovation in the case of TC Roke (2011) at $t = 3$ h, as indicated by rectangles in Figs. 4a and 4b. The introduced innovation had magnitude of +5 hPa with respect to the first guess, which should weaken the TC intensity.

Figure 4 illustrates the first-guess field at $t = 3$ h. The horizontal wind field at the ninth vertical level of the model ($z_h = 0.68$ km) indicates that the very strong wind blowing to the south of Japan and the air masses in the East China Sea and Japan Sea were directed toward the TC center (Fig. 4a). TC Roke seems to have affected the wind field across a broad area in the calculation domain. The potential temperature field around the TC at the 33rd vertical level ($z_h = 9.63$ km) is characterized by a warm core whose radius is about 200 km (Fig. 4b). The azimuthal mean of the tangential wind exhibits a maximum value of 41.5 m s^{-1} at r = 65 km (r represents the distance from the TC center) and $z_h = 0.68$ km, and the wind speed decreases as the height increases (Fig. 4c). A warm core at the TC center has a deep structure extending from the surface to $z_h = 16$ km and has a maximum value of 10.4 K at $z_h = 9.63$ km (Fig. 4d). These features are almost the same as those observed in the first-guess field at $t = 0$ h, except that the TC center was located about 40 km to the southwest (figures not shown).

Figures 5a–e illustrate the analysis increments of the potential temperature at the 33rd vertical level (z_h = 9.63 km) at $t = 0$ h obtained from the 4D-Var-based systems. In the 4D-Var-Bnmc system, the largest change occurs more than 1000 km south of the TC center, although the decrease in the potential temperature around the TC is as expected because of the TC weakening (Fig. 5a). In the 4D-Var-Benkf0 system, a notable decrease in the potential temperature occurs around the TC center with a crescent-shaped pattern (Fig. 5b). The value with the maximum decrease is −0.30 K, which is 4 times larger than the maximum decrease of −0.08 K obtained from the 4D-Var-Bnmc system. Aside from the changes near the TC center, there are many small patches far from the location of the observation, partly due to sampling noise resulting from the insufficient number of ensemble members. The analysis increments obtained from the 4D-Var-BenkfS and 4D-Var-BenkfN systems are similar to that obtained from the 4D-Var-Benkf0 system (Figs. 5c,d). However, the spatial variations are not rapid as in the 4D-Var-Benkf0 system, and

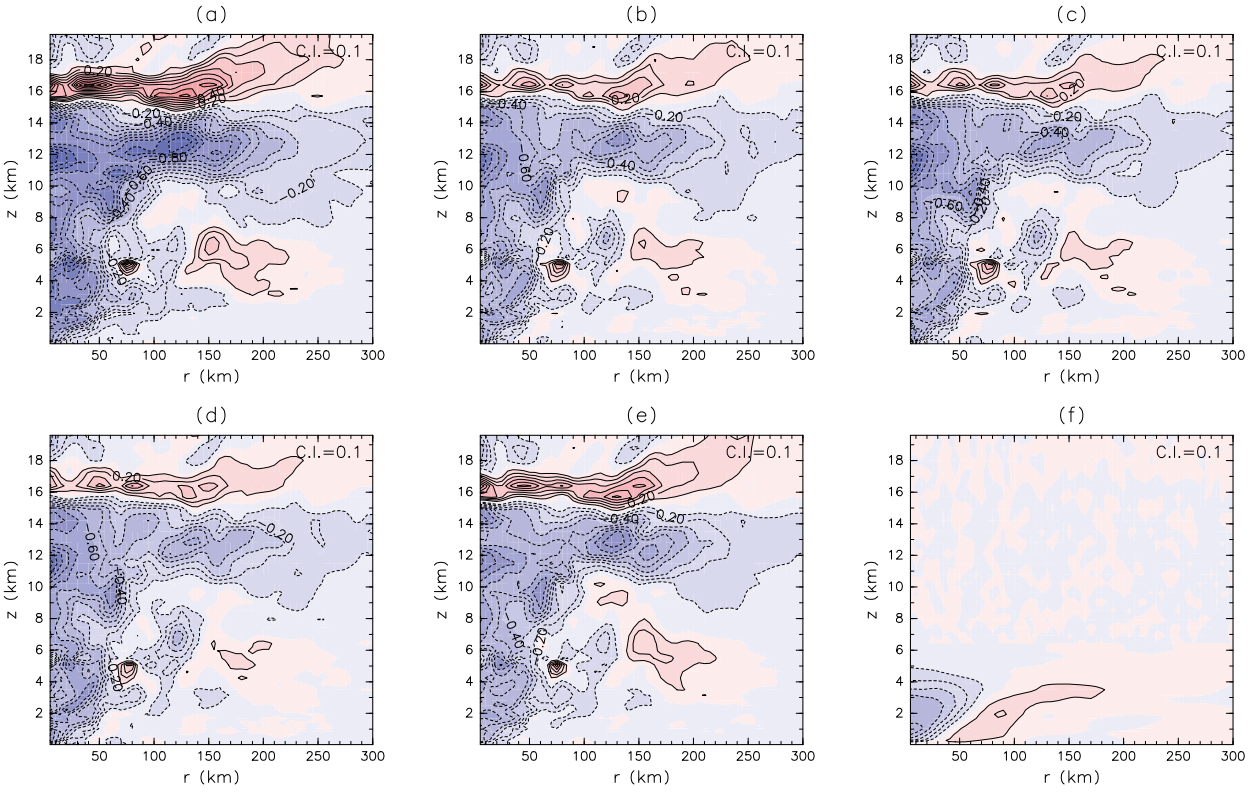

FIG. 8. (a)–(e) As in Figs. 6a–e, but at $t = 3$ h. (f) As in (a)–(e), but for LETKF analysis at $t = 3$ h.

very small-scale increment patches are slightly suppressed. The analysis increment obtained from the 4D-Var-BenkfL system is similar to that from the 4D-Var-Bnmc system, except for a notable change in the shape of the analysis increment near the TC center with the maximum decrease of −0.09 K (Fig. 5e). The contribution of the ensemble-based background error covariance $\sqrt{1-\beta}\delta\mathbf{x}_{\text{ens}}$ from Eq. (4) shows that the spatial localization approach significantly suppresses the analysis increment away from the observation location and that the spatial extent of decrease in the potential temperature is similar to the TC warm core size (Fig. 5f). The spatial localization approach efficiently reduces the estimated correlations for the large spatial separation more than the spectral localization and neighboring ensemble approaches do.

The azimuthally averaged feature in a storm-centered cylindrical coordinate shows that the analysis increment of the potential temperature by the 4D-Var-Bnmc system is characterized by large values at heights between the surface and 4 km (Fig. 6a). In contrast, the 4D-Var-Benkf0, 4D-Var-BenkfS, and 4D-Var-BenkfN increments weaken the warm core, in particular around heights of 8–12 km (Figs. 6b–d). Although the analysis increment obtained from the 4D-Var-BenkfL system is similar to that from the 4D-Var-Bnmc system (Fig. 6e), the ensemble-based part of the analysis increment exhibits a pattern similar to those obtained from the 4D-Var-Benkf0, 4D-Var-BenkfS, and 4D-Var-BenkfN systems, but with a different magnitude (Fig. 6f).

The magnitude of the analysis increment obtained from the 4D-Var-BenkfL system is substantially smaller with a maximum value in the lower troposphere near the TC warm core compared to those of the other hybrid systems, while the analysis increment forms a crescent-shaped pattern just east of the observation location as in the other hybrid systems. Because the difference between the 4D-Var-Benkf0 and 4D-Var-BenkfL systems resulted from a specified background error covariance matrix, the spatial localization was considered to suppress the magnitude of the analysis increment. To confirm this hypothesis, we conducted three analogous DA experiments by changing the setup of 4D-Var-BenkfL: in one, the horizontal localization scale was doubled (EXP_h2); in the next, the vertical localization was not applied (EXP_novert); and in the final experiment, the horizontal localization scale was doubled without the vertical localization (EXP_h2novert). In EXP_h2, the axisymmetric structure of analysis increment at $t = 0$ h is similar to that obtained from the original run in

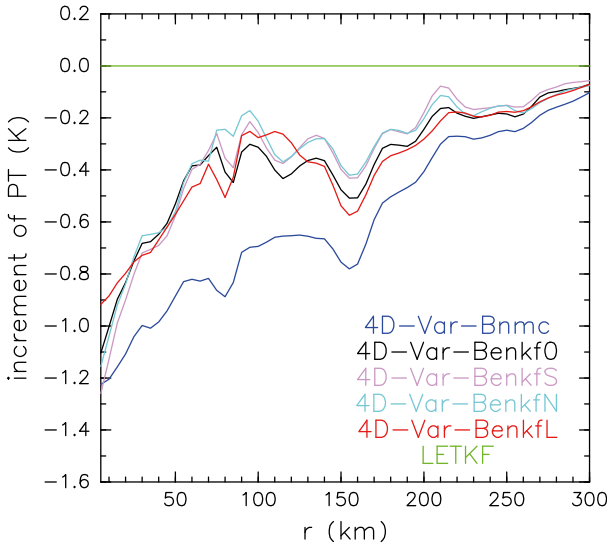

FIG. 9. Azimuthally averaged analysis increment of potential temperature at $z_h = 11.5$ km.

that it has a maximum decrease in the lower troposphere (Fig. 7a). In EXP_novert, a vertically deep structure appears around the TC center (Fig. 7b). The peak of the potential temperature analysis increment in the upper troposphere becomes more obvious in EXP_h2novert (Fig. 7c). These results indicate that, while a large potential temperature analysis increment in the upper troposphere is physically reasonable as a response to the innovation of sea level pressure in the TC, the vertical localization with the aid of the horizontal localization substantially suppresses the vertically coherent structure.

At the end of the assimilation window ($t = 3$ h), the analysis increment evolves in time according to the model dynamics during the assimilation window as shown in Fig. 2 of Kuhl et al. (2013) and Fig. 9 of Clayton et al. (2013). The azimuthally averaged analysis increments of the potential temperature field at $t = 3$ h are shown in Fig. 8. The increments derived from all of the 4D-Var-based methodologies exhibit similar patterns characterized by warm core weakening, negative potential perturbations in the upper troposphere, and increased potential temperatures in the lower stratosphere. The weakening of the warm core is consistent with the TC dynamics. Although the overall structures are similar among the 4D-Var-based methodologies, there are several differences between the increments of the 4D-Var-Bnmc and hybrid DA systems. For example, the horizontal coherence is rather strong in the 4D-Var-Bnmc increment compared with the increments obtained from the hybrid systems. Figure 9 shows that the potential temperature analysis increment at $z_h = 11.5$ km is similar among the hybrid systems in that its magnitude rapidly decreases from the center to $r = 100$ km. In contrast, the radial gradient of the potential temperature analysis increment is rather gentle up to $r = 300$ km with the use of the 4D-Var-Bnmc system. Moreover, vertical coherence is evident between 6 and 13 km at the TC center in the hybrid results, while it is not apparent in the 4D-Var-Bnmc results. These results indicate that the 4D-Var-Bnmc increment still tends to capture horizontal scales larger than those obtained from the hybrid systems and that the potential temperature increments of the hybrid systems are similar to each other at the end of the DA window. For reference, the analysis increment of the potential temperature that was derived from the LETKF system is shown in Fig. 8f. It is almost zero in the middle and upper troposphere, which does not have a vertically deep structure as in the 4D-Var-BenkfL system. This difference between 4D-Var-BenkfL and LETKF can be explained by considering the best linear unbiased estimates at $t = 0$ that are respectively written as

$$\delta\mathbf{x}_0 = \mathbf{M}_t(\mathbf{X}\mathbf{X}^{\mathrm{T}} \circ \mathbf{C})\mathbf{M}_t^{\mathrm{T}}\mathbf{H}_t^{\mathrm{T}} \times [\mathbf{R}_t + \mathbf{H}_t\mathbf{M}_t(\mathbf{X}\mathbf{X}^{\mathrm{T}} \circ \mathbf{C})\mathbf{M}_t^{\mathrm{T}}\mathbf{H}_t^{\mathrm{T}}]^{-1}(\mathbf{y}_t - \mathbf{H}_t\mathbf{M}_t\mathbf{x}_b) \quad (16)$$

and

$$\delta\mathbf{x}_0 = \mathbf{M}_t\mathbf{X}\mathbf{X}^{\mathrm{T}}\mathbf{M}_t^{\mathrm{T}}\mathbf{H}_t^{\mathrm{T}} \times (\mathbf{R}_t \circ \mathbf{C}' + \mathbf{H}_t\mathbf{M}_t\mathbf{X}_t\mathbf{X}^{\mathrm{T}}\mathbf{M}_t^{\mathrm{T}}\mathbf{H}_t^{\mathrm{T}})^{-1}(\mathbf{y}_t - \mathbf{H}_t\mathbf{M}_t\mathbf{x}_b), \quad (17)$$

where $\mathbf{C}'$ denotes the diagonal matrix. Each element of $\mathbf{C}'$ is the inverse of the localization weight determined by r_o (Hunt et al. 2007; Miyoshi and Yamane 2007). The analysis increment is set to completely zero in LETKF where an analysis grid point is more than $2\sqrt{10/3}r_o$ away from the observation location. In the 4D-Var-BenkfL system, it is not necessarily zero even at an analysis grid point away from an observation location because the localization scale is defined by r_a and the analysis increment evolves in time according to the model dynamics. Similar difference between 4D-Var and LETKF was also observed in Yokota et al. (2016).

In sum, the analysis increment differs largely between the 4D-Var-Bnmc and hybrid methods at the beginning of the assimilation window. At the end of the assimilation window, the analysis increments become closer to each other partly because of the time evolution according to the model dynamics, and their structures are physically reasonable. Nevertheless, there still remain differences between the analysis increments of the 4D-Var-Bnmc and hybrid methods; for example, the

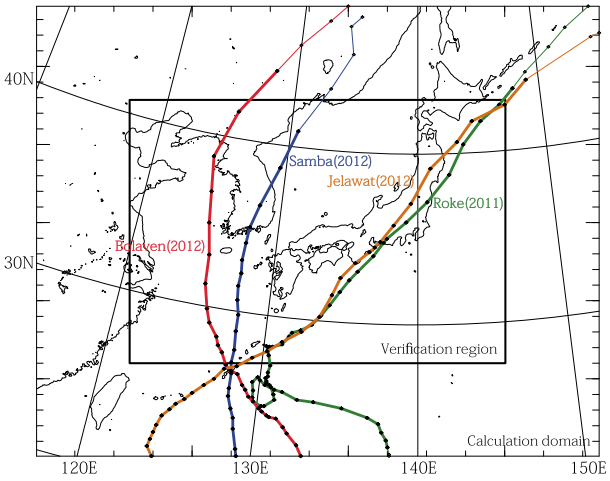

FIG. 10. RSMC best track of TCs investigated in this study (thick lines). Thin lines indicate the track for an extratropical cyclone that was a former TC.

4D-Var-Bnmc increment tends to have a stronger horizontal coherence. In this section, we have not discussed the analysis increment of the velocity field. Briefly speaking, the hybrid DA systems yielded anticyclonic circulation consistent with the dynamics of a mature TC at the beginning of the assimilation window. The analysis increment derived from 4D-Var-Bnmc exhibited both cyclonic and anticyclonic circulation patterns at the beginning. This 4D-Var-Bnmc increment formed an anticyclonic vortex at the end, while the horizontal coherence is relatively large (figures not shown). Note that here the analysis increment was only investigated in response to MSLP in one cycle. In realistic DA configurations, observations in different locations and during multiple cycles propagate error information to broad regions in the calculation domain.

4. TC forecasts

a. Selected events

To investigate the quality of each DA system, we selected the four TCs that were the strongest in 2011–12 in terms of the MSLPs reported by the Regional Specialized Meteorological Center (RSMC) Tokyo within the calculation domain: TCs Roke (2011), Bolaven (2012), Samba (2012), and Jelawat (2012). The center positions in the RSMC best tracks are shown in Fig. 10, while the experimental periods and peak intensities are summarized in Table 1. We validated only the events in which all of the systems reproduced TCs at the verification time within the verification region described in the best track for fair comparison (see Fig. 10). The total numbers of cases for verification were 62, 61, 57, and 51 for forecast times of 0 (analysis), 12, 24, and 36 h, respectively.

b. Forecast quality

The mean errors (MEs) of the TC track forecasts along with the root-mean-square errors (RMSEs) of the forecasted MSLPs and maximum wind speeds at 10-m height (Vmax) for the four TCs are shown in Fig. 11. The position errors are smaller for the forecasts initialized by the LETKF and hybrid systems than they are for those initiated by the 4D-Var-Bnmc system at forecast times equal to and longer than 6 h (Fig. 11a). The track forecast errors at 24 h are improved by about 10%. It is intriguing that the forecast errors are similar to each other among the LETKF and hybrid experiments. In the TC intensity predictions, the LETKF error is initially larger than the errors of the results obtained from the other DA methods, and the 4D-Var-Bnmc-based initial conditions caused the error to increase rapidly with increasing forecast time up to 9 h. The intensity errors in the forecasts initialized by the hybrid systems are smaller than those of the forecasts initialized by the 4D-Var-Bnmc and LETKF systems.

The results of t tests for the position errors and the squared errors of MSLP and Vmax indicate that the improvements over the 4D-Var-Bnmc system by using the hybrid systems are generally statistically significant (Fig. 12). The LETKF system is generally more accurate than the 4D-Var-Bnmc model in terms of track prediction, although it is not necessarily superior in terms of intensity prediction. Note that this does not indicate that LETKF is inferior to 4D-Var-based methodologies because the LETKF system employed the coarse resolution of 15 km as well as an ensemble average on the geographically fixed coordinate.

To understand the quality of track prediction, the steering flow was calculated because it is closely related to

TABLE 1. List of TCs investigated in this study. MSLP and Vmax indicate the peak values during the verification period (1 kt = 0.5144 m s^{-1}).

TC name	Initial time	End time	MSLP (hPa)	Vmax (kt)
Roke (2011)	0900 UTC 20 Sep	0000 UTC 22 Sep	940	85
Bolaven (2012)	1800 UTC 26 Aug	1800 UTC 28 Aug	940	80
Samba (2012)	0000 UTC 16 Sep	1800 UTC 17 Sep	935	90
Jelawat (2012)	0900 UTC 29 Sep	0600 UTC 1 Oct	935	90

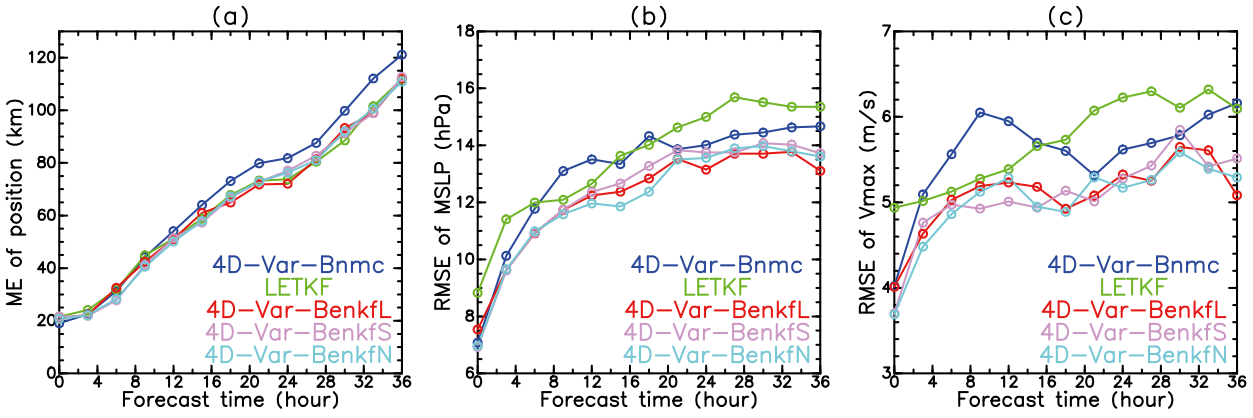

FIG. 11. (a) ME of track, and RMSE of (b) MSLP and (c) Vmax with respect to RSMC Tokyo best track. Results obtained using 4D-Var-Bnmc, LETKF, 4D-Var-BenkfL, 4D-Var-BenkfS, and 4D-Var-BenkfN systems are indicated by blue, green, red, light purple, and cyan, respectively.

TC motion (Elsberry 1995). The steering flow was defined as the mean wind vector between 850 and 300 hPa within a 600 km × 600 km rectangle centered at the TC center position, which is the same as the definition used by Wu et al. (2007). The composite mean of the steering flow (u, v) is shown in Fig. 13. The zonal wind seems to be a bit different at the initial time (Fig. 13a), though the meridional component of the steering flow shows weaker southerly wind at the initial time in the analysis obtained from the LETKF and hybrid systems unlike in that obtained from the 4D-Var-Bnmc system (Fig. 13b). It is consistent with the similarity in the position errors initialized by the LETKF and hybrid systems.

The composite means of the meridional wind fields around the TCs in the 4D-Var-Bnmc system indicate cyclonic circulation (Fig. 14a). The southerly winds to the east of the TCs are generally stronger than the northerly winds to the west partly because the northward translation speed was added to the cyclonic wind field associated with the TC motion. The difference in the hybrid systems relative to the 4D-Var-Bnmc system show that the cyclonic circulation becomes stronger in an inner core region and the southward wind anomalies appear in the surrounding area (Figs. 14b–d). This southward wind anomaly in the surrounding area is also observable in the LETKF result. Comparison of the 4D-Var-Bnmc and LETKF analysis increments further

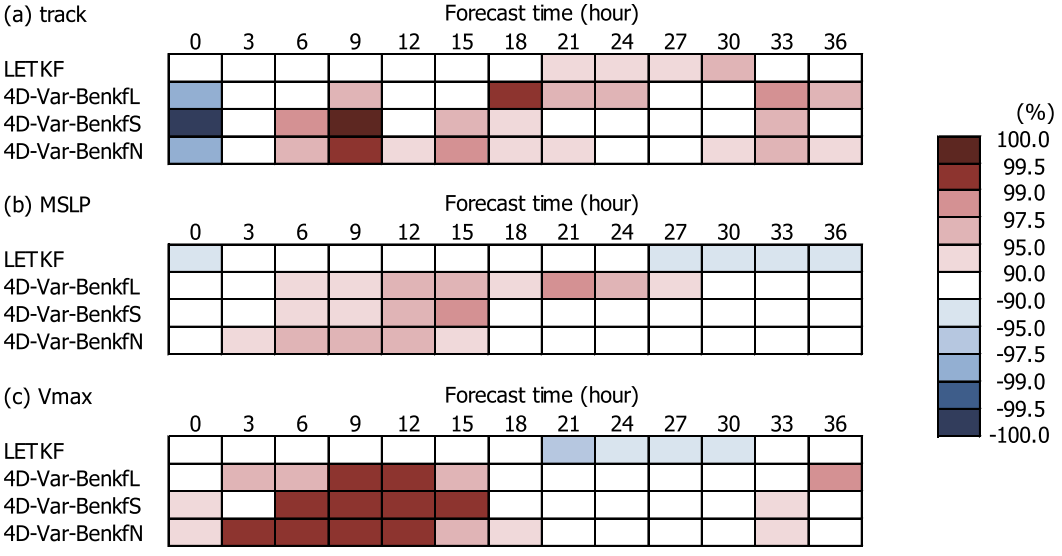

FIG. 12. Results of two-tailed paired sample t tests for (a) track error, (b) squared MSLP error, and (b) squared Vmax error. Shadings in red (blue) indicate improvement (degeneration) in forecasts initialized by LETKF, 4D-Var-BenkfL, 4D-Var-BenkfS, and 4D-Var-BenkfN systems with respect to 4D-Var-Bnmc system.

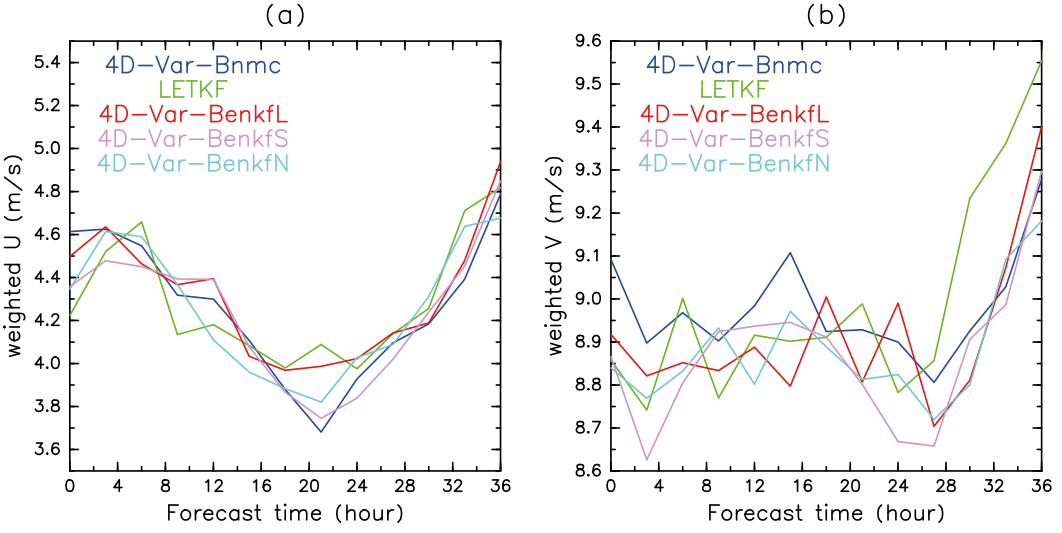

FIG. 13. (a) Composite of zonal component of steering flow. (b) As in (a), but for meridional component. See section 4b for definitions. Line colors are identical to those used in Fig. 11.

reveals that a larger TC vortex was reproduced by the LETKF system, which shows cyclonic (anticyclonic) circulation outside (inside) the radius at which the maximum wind occurs in the 4D-Var-Bnmc system (Fig. 14e). Therefore, the changes in the inner core structure differ between the LETKF and hybrid systems, while their resultant steering flows, defined as the 600 km × 600 km area-averaged winds, both exhibit southward wind anomalies relative to the 4D-Var-Bnmc results.

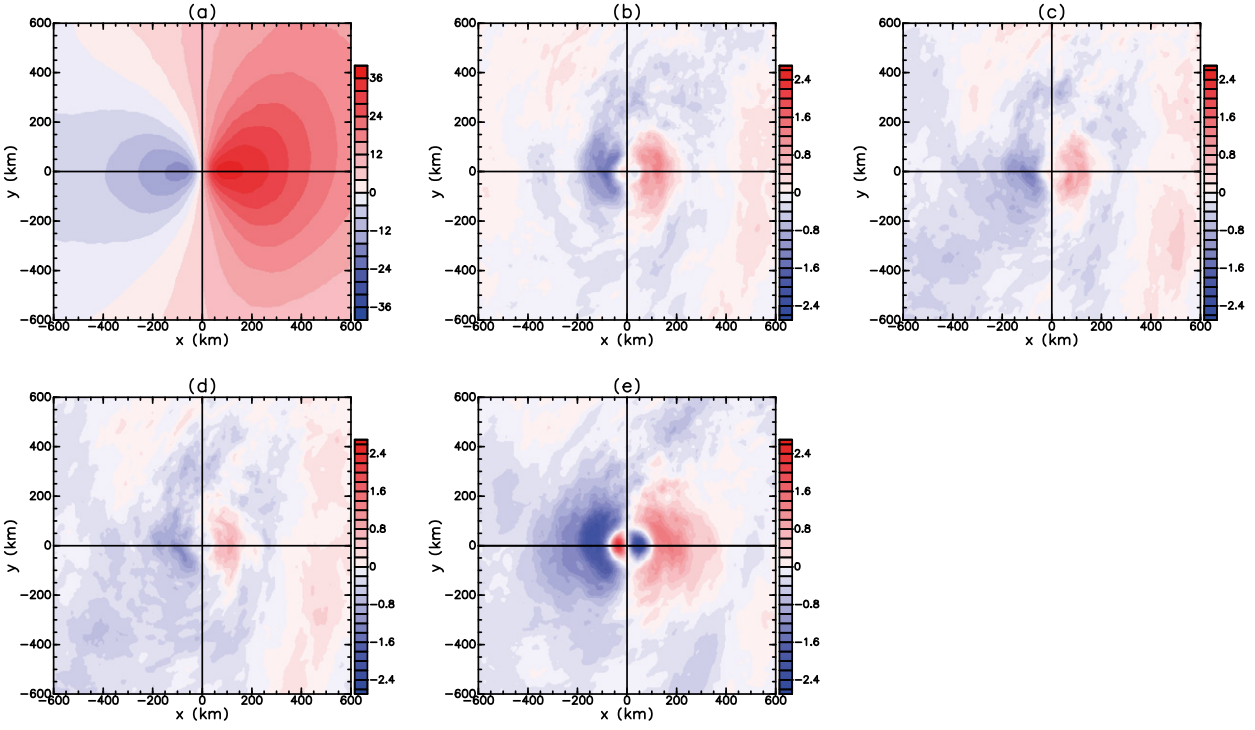

FIG. 14. (a) Composite of meridional wind in 4D-Var-Bnmc analysis. (b) Composite of meridional wind anomaly in the 4D-Var-BenkfL analysis relative to the 4D-Var-Bnmc analysis. (c)–(e) As in (b), but for 4D-Var-BenkfS, 4D-Var-BenkfN, and LETKF analyses, respectively, relative to 4D-Var-Bnmc analysis.

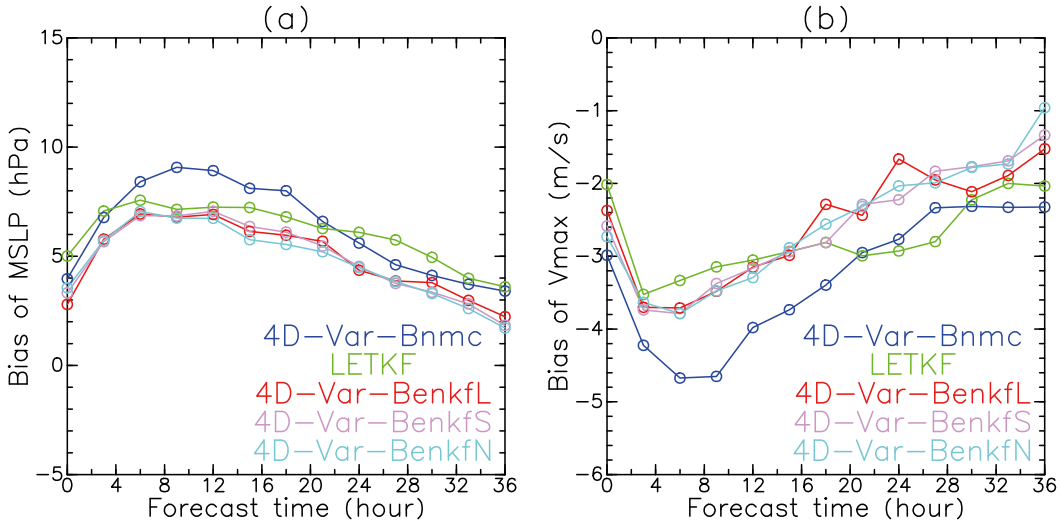

FIG. 15. Composite mean bias for (a) MSLP (hPa) and (b) Vmax ($m\,s^{-1}$) at each forecast time obtained from each DA system.

We proceeded to investigate the mean biases in the TC intensity forecasts because the RMSE is the square root of the sum of the squared mean bias and residual. Figure 15 shows the mean biases of MSLP and Vmax. In general, the TCs are weakly reproduced at the initial time in all of the systems. Among them, the MSLP has a large positive bias and the Vmax has a large negative bias in the 4D-Var-Bnmc results from $t = 3$ to $t = 12$ h, contributing to the worse intensity forecast score (Figs. 11b,c). Figure 16 shows that the composite mean of the radius of maximum wind (RMW) tends to become large after 3 h when initial state is given by the 4D-Var-Bnmc system. This increase in the RMW is consistent with the excessive weakening of the TC intensity because of the quasi-conservation of absolute angular momentum, which is approximately proportional to the tangential velocity times the radius in the TC inner core. This rapid increase of the RMW is not evident in the RMWs of the LETKF and hybrid results. This enlargement of RMW may be related to the nature of the 4D-Var-Bnmc system, which tends to distribute more energy to a broad region away from the TC center, as described in section 3.

Figure 17 shows the MSLP analysis compared to the RSMC best track. The MSLP analysis agrees well with the RSMC values for weak TCs. However, the intensities of strong TCs are not fully reproduced; in particular, the analysis of MSLPs obtained using the LETKF system is sometimes above 960 hPa, even when the actual MSLP is less than or equal to 940 hPa. These differences are presumably evident because the 15-km grid spacing (used in the simplified nonlinear model of the 4D-Var system and the LETKF system) is not sufficient to resolve the inner core structure of an intense TC (Gentry and Lackmann 2010) and because of the potential issue of simplified and/or linearized physics even with a bogus TC assimilation. This situation might be improved in the 4D-Var-based methodologies that employ horizontal grid spacings of 5 km in the high-resolution model. In addition, the spatially sharp structures of the variables are lost in the LETKF system because the analysis is performed using the geographically fixed ensemble mean of the peak values reproduced at the different location in each realization. This characteristic caused the mean RMWs of the TCs in the LETKF analysis to be larger than those obtained using the 4D-Var-based methodologies by about 10 km (Fig. 16) and also caused the horizontal wind fields associated with the TCs to become broader (Fig. 14e).

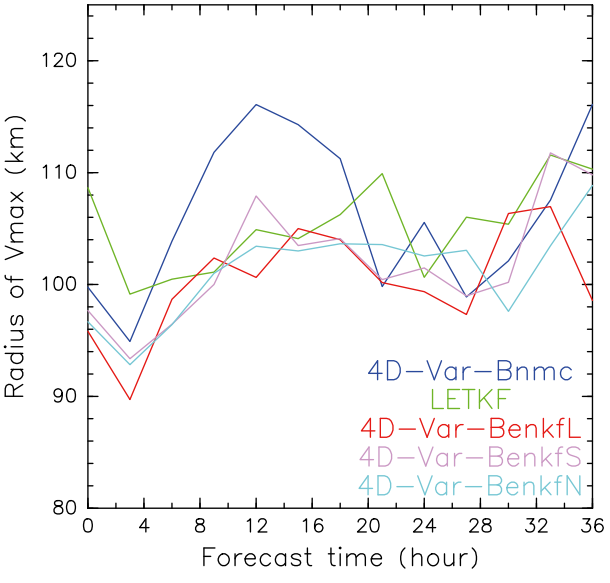

FIG. 16. As in Fig. 13, but for composite of RMW.

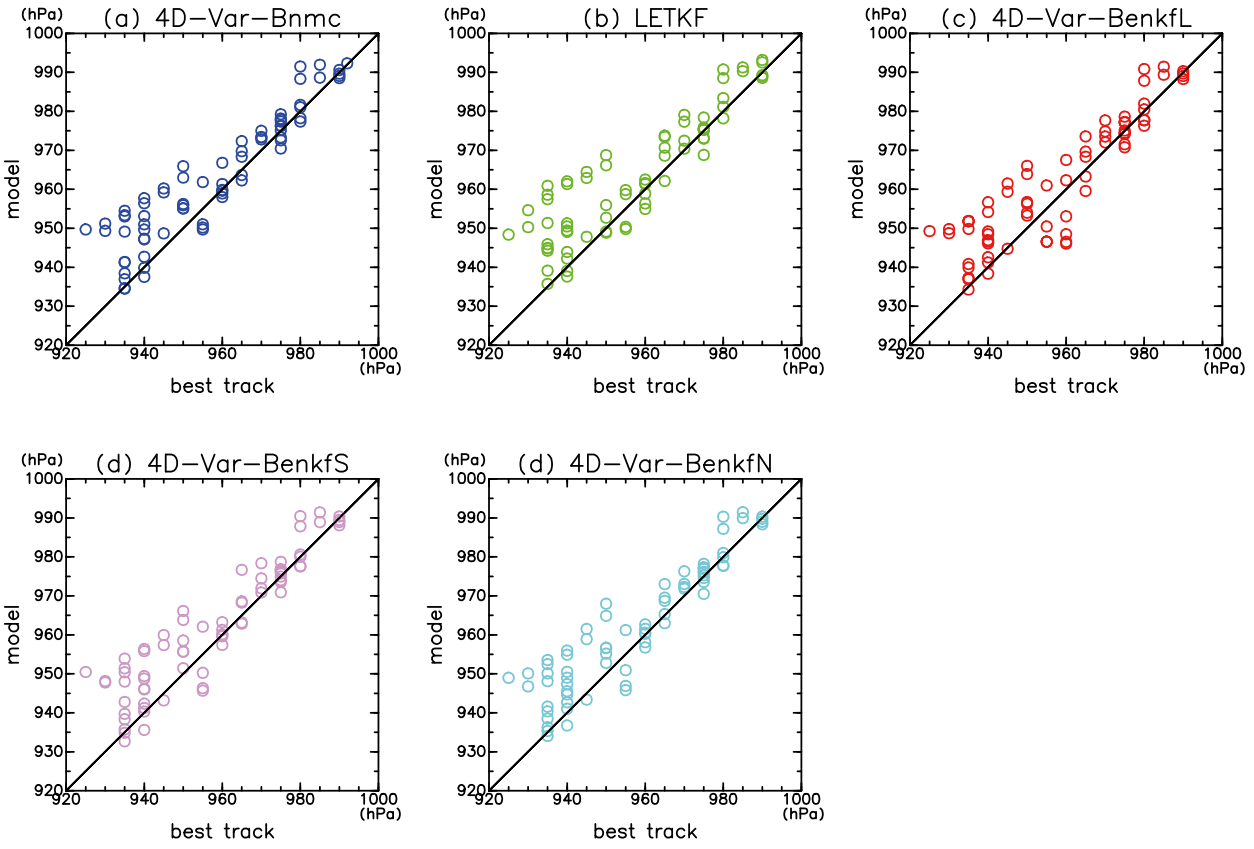

FIG. 17. MSLP in RSMC best track and corresponding (a) 4D-Var-Bnmc, (b) LETKF, (c) 4D-Var-BenkfL, (d) 4D-Var-BenkfS, and (e) 4D-Var-BenkfN analyses.

It is notable that all of the hybrid systems yield TC track, MSLP, and Vmax predictions with similar skills and that these predictions are more accurate than those obtained from the 4D-Var-Bnmc system, even though the strategies of constructing $\mathbf{B}_{\text{ens}}$ are rather different. This fact is supported by the similarity between their steering flow structures, potential temperatures, humidity profile, and RMWs (figures for potential temperature and humidity profile are not shown).

5. Local heavy rainfall events

a. *Selected events*

Local heavy rainfall events have sometimes caused flooding and debris flows that have killed many people. The JMA designated three events as rainfall-related disasters[3] in 2011–12; these disasters occurred in Niigata–Fukushima (2011), northern Kyushu (2012), and Kinki (2012) (http://www.data.jma.go.jp/obd/stats/data/bosai/report/index_1989.html). In this work, we applied the DA systems to initialize the forecasts for these torrential rainfall events, whose locations are shown in Fig. 18a. In each case, the frontal zone was located near the areas of local heavy rainfall. Warm and humid winds flowed along these fronts, which brought torrential rainfall (Figs. 18b–d).

Kunii (2014) showed that the northern Kyushu heavy rainfall event could have been predicted better at forecast times of 12 and 24 h by using an initial state obtained from the LETKF system compared with the 4D-Var-Bnmc system. Nevertheless, hybrid systems have never been applied to these events. The forecast experiments are verified during the periods of torrential rainfalls reported by the JMA as dates (in local standard time) shown in Table 2. Verification periods are 4 days (96 h), 4 days (96 h), and 2 days (48 h) for the Niigata–Fukushima area (2011), northern Kyushu region (2012), and Kinki region (2012) events, respectively. The initial forecast times were every 3 h between 24 h prior to the beginning of the verification time and 3 h prior to the end of the verification time. A total of 104 forecast experiments were initialized by each DA system.

[3] Rainfall events associated with TCs were excluded.

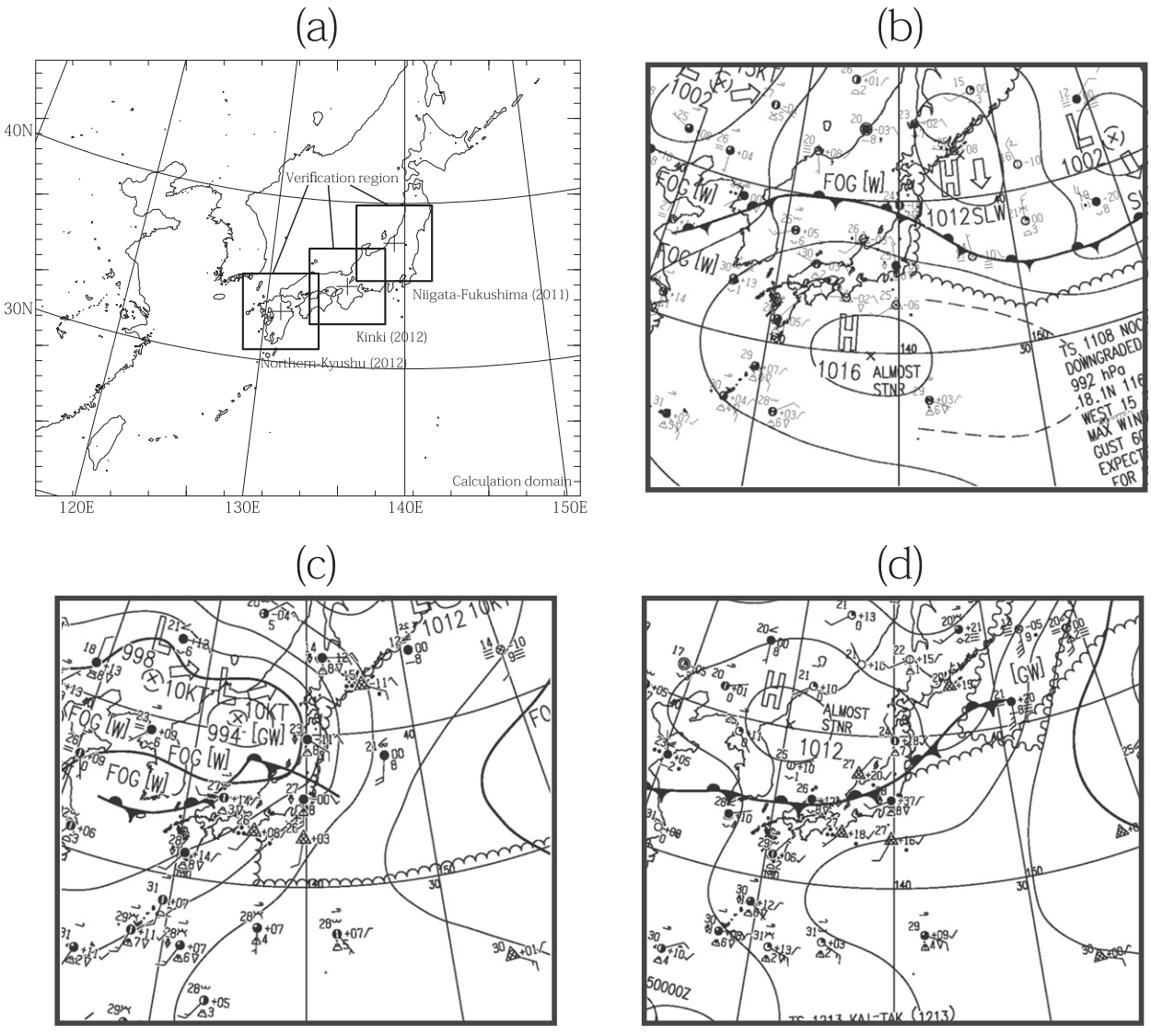

FIG. 18. (a) Verification region for local heavy rainfall events investigated in this study. Squares indicate verification region of 500 km on each side centered at location of maximum total rainfall in each event. (b)–(d) Surface weather maps produced by JMA at 0000 UTC 28 Jul 2011, 0000 UTC 12 Jul 2012, and 0000 UTC 14 Aug 2012, respectively.

b. Forecast quality

Figure 19 shows the RAP analysis of the total accumulated rainfall during the verification period[4] for the heavy rainfall event in Niigata–Fukushima (2011) and the corresponding model forecasts initialized by all the DA systems. To compare with the RAP analysis, we compiled model-derived 3-h accumulated rainfall amounts at forecast times of 30–33 h. The total rainfall amount is also shown for the event in northern Kyushu (2012) (Fig. 20). All of the systems predicted the peak total rainfall amount to be more than 400 mm for the Niigata–Fukushima and northern Kyushu events. Thus, the occurrence of unusual local heavy rainfall was successfully predicted regardless of the choice of a DA scheme, although the total rainfall amount was generally underestimated in the model forecasts. The optimum initialization scheme in terms of predicting the peak rainfall locations differs among the events. For the Niigata–Fukushima event, the peak rainfall location was predicted reasonably well by the hybrid-based initial

[4] The data for the first 6 h from the beginning of the verification time are excluded from this plot. Because the forecast initial time begins 24 h prior to the verification time, the corresponding model outputs at forecast times of 30–33 h are not available.

TABLE 2. List of local heavy rainfall events investigated in this study.

Event name	Initial day	End day	Total rainfall (mm)	Max 3-h rainfall (mm)
Niigata–Fukushima (2011)	27 Jul	30 Jul	711.5	167.0
Northern Kyushu (2012)	11 Jul	14 Jul	816.5	288.5
Kinki (2012)	13 Aug	14 Aug	228.5	109.5

condition, while it was incorrectly reproduced far to the west of the actual location by the LETKF-based initial condition. In contrast, the peak rainfall location was predicted reasonably by using the LETKF system for initialization for the northern Kyushu event, while the 4D-Var-Bnmc system yielded the peak location in the southern part of Kyushu Region. The better skill of LETKF for the northern Kyushu event is consistent with the results of Kunii (2014).

To evaluate the forecast quality of heavy rainfall events over several experimental cycles, the threat score (TS) and fractions skill score (FSS) were used (Duc et al. 2013; Ebert 2009; Wilks 2011). TS is defined as

$$\mathrm{TS} = \frac{H}{H + F + M}, \tag{18}$$

where F is the number of points at which the predicted precipitation corresponds to a false alarm, M is the number of points at which the observed precipitation was missed by the prediction, and H is the number of successful predictions. TS ranges from 0 to 1, where TS = 1 means a perfect forecast. FSS is defined as

$$\mathrm{FSS} = 1 - \frac{\sum_{j=1}^{N} (p_j - o_j)^2}{\sum_{j=1}^{N} (p_j)^2 + \sum_{j=1}^{N} (o_j)^2}, \tag{19}$$

where the forecast fraction p and observation fraction o are computed by taking the ratio between the number of occurrences of the event of interest and the number of grid points inside a spatial window. The index j runs over

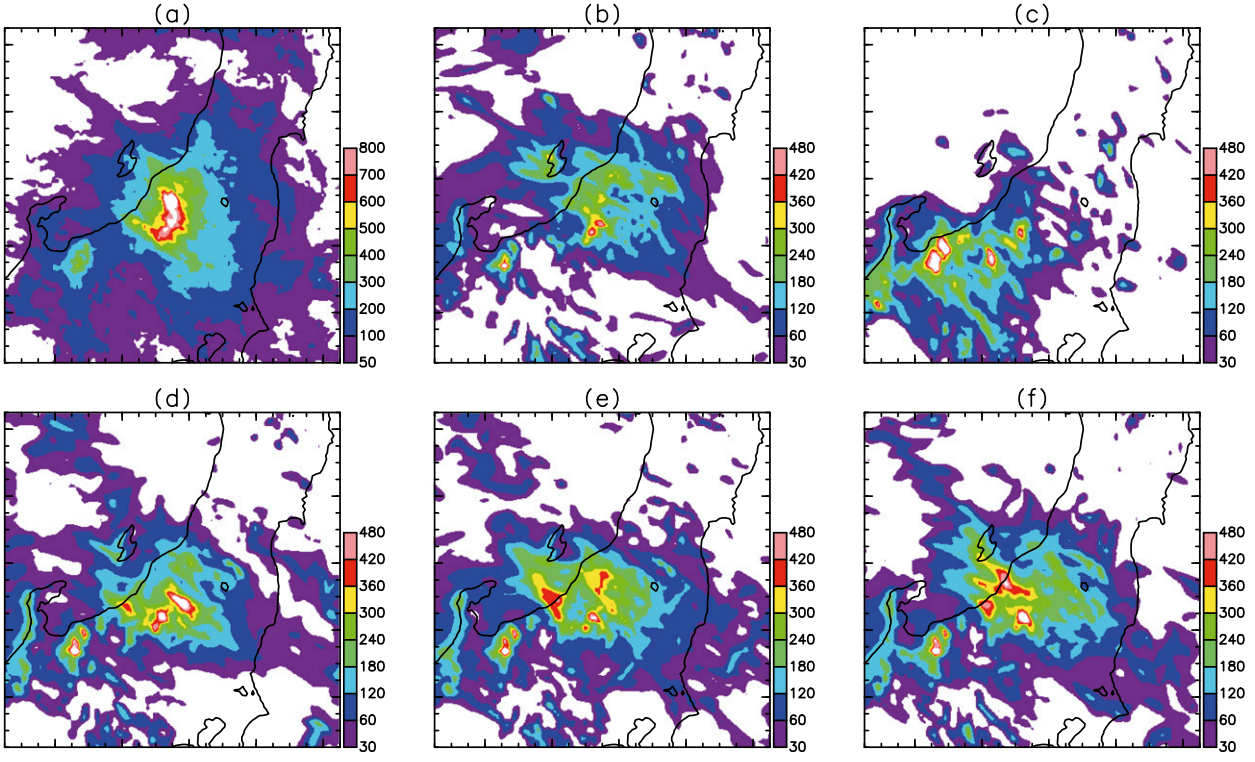

FIG. 19. Total accumulated rainfall amount within verification region for the local heavy rainfall event in Niigata–Fukushima area (2011). (a) RAP analysis. (b) Total rainfall amounts corresponding to (a) in the model forecasts initialized by 4D-Var-Bnmc system. Forecasts were constructed by integration of 3-h accumulated rainfall at forecast times of 30–33 h. (c)–(f) As in (b), but for model forecasts initialized by (c) LETKF, (d) 4D-Var-BenkfL, (e) 4D-Var-BenkfS, and (f) 4D-Var-BenkfN systems.

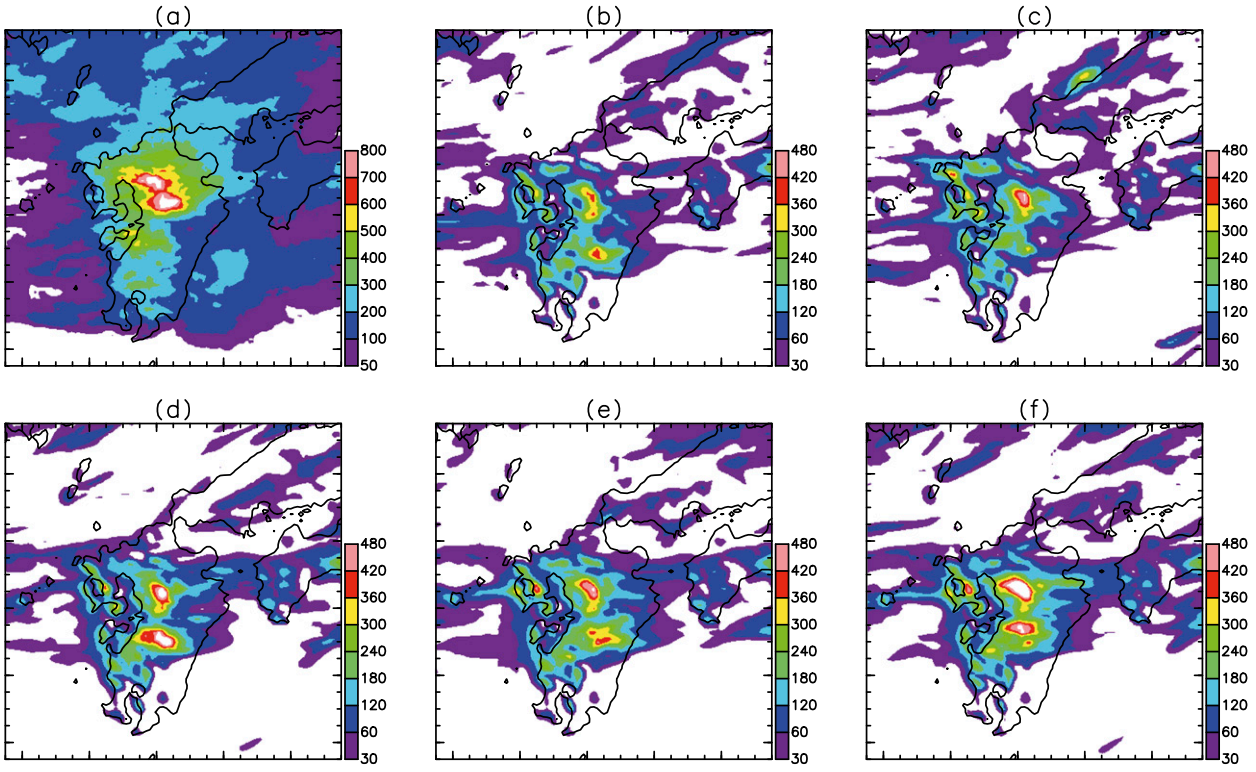

FIG. 20. As in Fig. 19, but for the local heavy rainfall event in northern Kyushu region (2012).

all pixels inside the verification area, and this N is the total number of grid points inside a verification area. FSS ranges from 0 to 1, where FSS = 1 means a perfect forecast. In contrast to the strict requirement of TS evaluating the exact point–point match, FSS relaxes this requirement between the forecasts and the observations by taking adjacent grid points into account; thus, it can be used to verify the quality of a precipitation forecast from a coarse-grained view. Here, we verified the model output by comparing it to RAP data that were obtained on land within the verification region of 500 km × 500 km centered at the location of maximum total accumulated rainfall over the verification periods, as shown in Fig. 18.

Figures 21a–c show TS for 3-h accumulated rainfall at forecast times of 6–9, 15–18, and 33–36 h. Notably, the hybrid systems exhibit no clear improvements compared to the 4D-Var-Bnmc system at any forecast time. Comparison between the LETKF-based and 4D-Var-based forecasts indicates that TS is smaller in the LETKF-based forecasts by up to 25 mm $(3\,\mathrm{h})^{-1}$. This feature has also been observed in previous studies (Kunii 2014; Saito et al. 2011). In general, the differences (relative to the 4D-Var-Bnmc method) are statistically neutral, except for the degeneration of the weak rainfall prediction accuracy initialized by the LEKTF system (figures not shown). Please note that the worse skill of LETKF may come from a coarse resolution of 15 km and the use of a geographically fixed ensemble mean.

The behavior of FSS with a window size of 20 km × 20 km is similar to that of TS, indicating that the quality of forecasts initialized by the different DA methodologies does not differ as a result of smoothing the horizontal scale over this spatial range (Figs. 21d–f). The behavior of FSS with a window size of 160 km × 160 km is generally improved for forecast times of 33–36 h in the hybrid-based forecasts compared to the 4D-Var-Bnmc-based forecasts, while the 4D-Var-Bnmc system provides reasonable estimates in terms of predicting very intense rainfall for forecast times of 15–18 h. Therefore, the evaluation of the heavy rainfall predictions can be changed by taking a coarse-grained view on this horizontal scale, although grid-scale prediction of the exact location yields no improvement, perhaps because of its extreme difficulty (Duc et al. 2013). Figure 22 shows the results for the statistical significance test of FSS for 3-h accumulated rainfall with a window size of 160 km × 160 km. All of the hybrid DA systems sometimes provide initial conditions that yield forecasts at 0–6 and 30–36 h that are statistically more accurate than those of the 4D-Var-Bnmc system, while the changes were not detected as statistically significant improvements at other

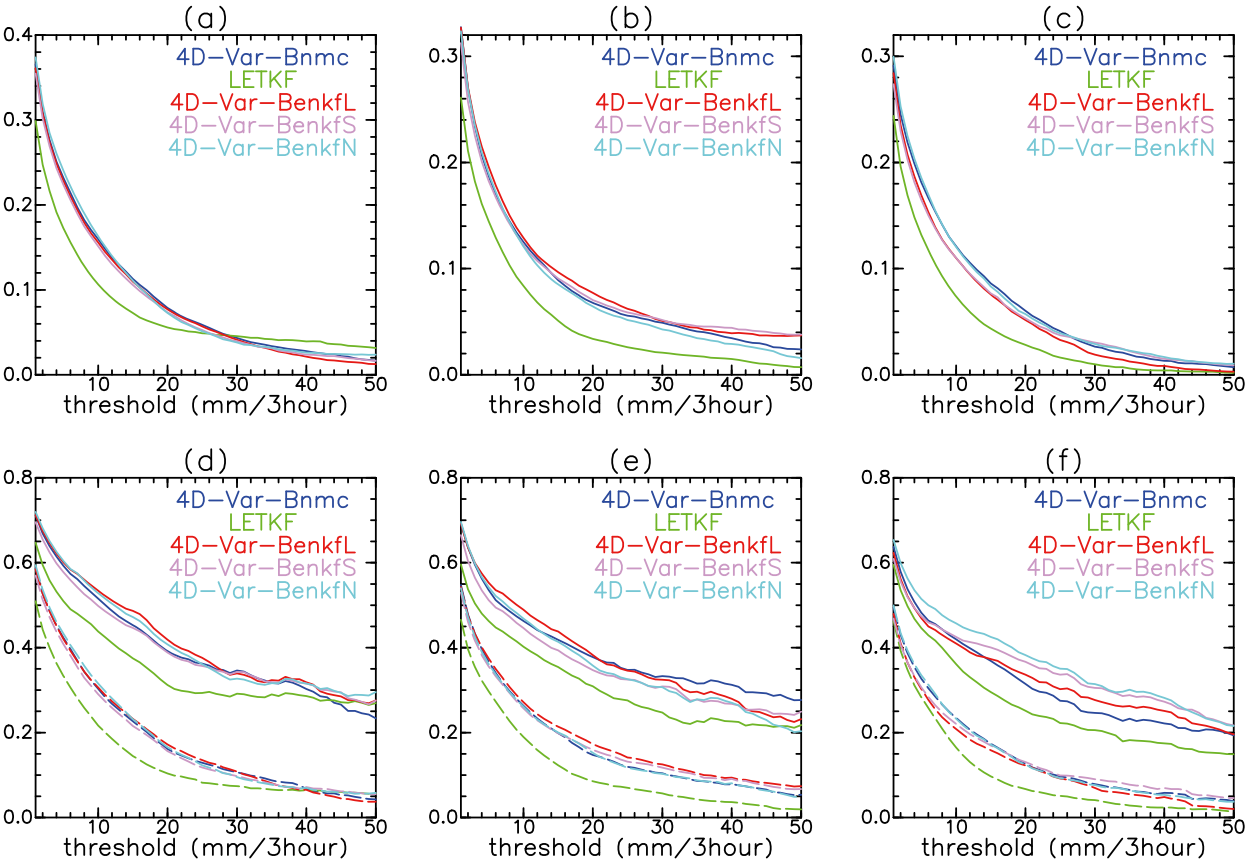

FIG. 21. (a) TS for 3-h accumulated rainfall during at forecast times between 6 and 9 h initialized by 4D-Var-Bnmc, LETKF, 4D-Var-BenkfL, 4D-Var-BenkfS, and 4D-Var-BenkfN systems. (b),(c) As in (a), but for 15–18 and 33–36 h, respectively. (d)–(f) As in (a)–(c), but for FSS. Solid and broken lines in (d)–(f) correspond to scores for 160 km × 160 km and 20 km × 20 km windows, respectively. These results are averaged over all the available cycles.

forecast times. It is possible that hybrid DA systems can generate the initial condition to predict local heavy rainfall events. However, further experiments are necessary to confirm the current findings with certainty.

6. Summary

To predict hazardous events accurately, the modeling of background error covariances should be more sophisticated. Therefore, we developed three hybrid mesoscale DA systems (spatial localization, spectral localization, and neighboring ensemble approaches) that use flow-dependent covariances constructed from the perturbations in the LETKF system. The adjoint-based 4D-Var system used is almost identical to the JMA operational regional DA system.

The single-observation assimilation experiment showed that the analysis increments obtained from the hybrid systems at the beginning of the assimilation window were physically reasonable. In contrast, the analysis increment obtained from the 4D-Var-Bnmc method did not capture TC-related features. At the end of the 3-h assimilation window, the TC-related features were captured by the analysis increments from both the hybrid DA and 4D-Var-Bnmc systems. Nevertheless, there were still some differences, for example, the 4D-Var-Bnmc increment was more horizontally coherent.

The realistic-DA experiments showed that hybrid-based initial conditions yielded TC track predictions and intensity forecasts that were more accurate than those obtained using 4D-Var-Bnmc-based initial conditions. LETKF-based initial conditions also yielded track forecasts that were more accurate than those resulting from 4D-Var-Bnmc-based initial conditions, while they did not improve the forecast quality of TC intensity. In general, these results were found to be statistically significant. We also applied these DA systems to initialize the predictions of three local heavy rainfall events that occurred in Japan in 2011–12. Although a relatively large number of forecast experiments (104 cycles) were performed, the hybrid DA systems exhibited no clear improvements over the 4D-Var-Bnmc system when TS was employed as a metric.

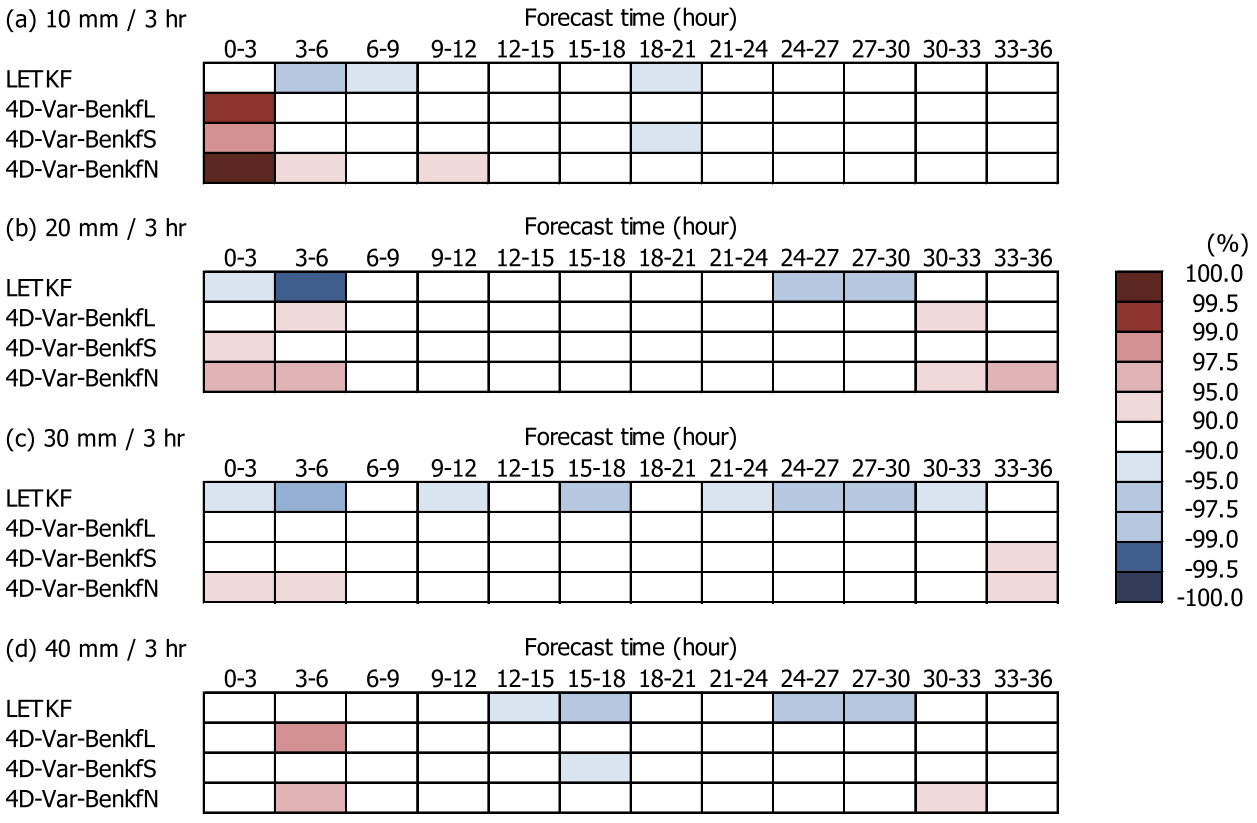

FIG. 22. As in Fig. 12, but for FSS with window size of 160 km × 160 km in terms of prediction skill of 3-h accumulated rainfall in which thresholds are (a) 10, (b) 20, (c) 30, and (d) 40 mm $(3\ \text{h})^{-1}$. Red (blue) indicates improvement (degeneration) in forecast quality relative to initialization by using 4D-Var-Bnmc system.

Another metric, FSS, indicated that initial conditions obtained from the hybrid DA systems yielded some improvements in predictions at forecast times of 0–6 and 30–36 h when a window size of 160 km × 160 km was used. However, more experiments are needed to confirm the improvements in the prediction of local heavy rainfall events. It is worth noting that the hybrid DA system employing the different strategies for suppressing the sampling noise exhibited similar quality in terms of predicting these severe weather events.

One may wonder why the LETKF system performs differently than the 4D-Var-based methodologies. Care should be taken when comparing the 4D-Var-based and LETKF methodologies because their model physics, observation binning, and configurations are not completely the same. In particular, the 4D-Var-based methodologies use the high-resolution model with grid spacings of 5 km to generate analysis increments, while the analysis field in the LETKF system has a grid spacing of 15 km. This difference could be the reason that the 4D-Var-based initialization is more accurate in very short term predictions of heavy rainfall than the initialization from an ensemble mean state of LETKF. Moreover, a TC simulation starting from a single member in the LETKF model could yield forecasts that are more accurate than those achievable by performing analysis defined by the ensemble mean state (Chang et al. 2014), which should be investigated in the future.

Acknowledgments. We thank Mr. Y. Yokota, Y. Honda, H. Tsuguti, and S. Kanda and Drs. T. Kato, T. Tsuyuki, H. Seko, T. Miyoshi, and T. Oizumi for providing useful comments. We also thank the Numerical Prediction Division of the JMA for providing the parallel L-BFGS program. This work was supported by the Ministry of Education, Culture, Sports, Science and Technology (MEXT) through the Strategic Programs for Innovative Research (SPIRE) and the FLAGSHIP2020, MEXT within the priority study4 (Advancement of meteorological and global environmental predictions utilizing observational "Big Data") using computational resources of the K computer provided by the RIKEN Advanced Institute for Computational Science through the HPCI System Research Project (Project ID: hp120282, hp130012, hp140220, hp150214, hp150289, and hp160). This project was also funded by MEXT KAKENHI Grants 16H04054

and 15K05294. This research was initially developed using the Fujitsu PRIMEHPC FX10 System (Oakleaf-FX) in the Information Technology Center, the University of Tokyo. The figures were produced by GFD-DENNOU Library.

REFERENCES

Aonashi, K., K. Okamoto, M. Yamaguchi, and S. Origuchi, 2013: Dual scale neighboring ensemble approach for the cloud-resolving model ensemble variational assimilation. *Sixth WMO Symp. on Data Assimilation*, College Park, MD, University of Maryland, 7.4. [Available online at http://das6.umd.edu/program/Daily/abs/7.4-Aonashi_Kazumasa.pdf.]

Bishop, C. H., D. Hodyss, P. Steinle, H. Sims, A. M. Clayton, A. C. Lorenc, D. M. Barker, and M. Buehner, 2011: Efficient ensemble covariance localization in variational data assimilation. *Mon. Wea. Rev.*, **139**, 573–580, doi:10.1175/2010MWR3405.1.

Bonavita, M., L. Isaksen, and E. Hólm, 2012: On the use of EDA background error variances in the ECMWF 4D-Var. *Quart. J. Roy. Meteor. Soc.*, **138**, 1540–1559, doi:10.1002/qj.1899.

Buehner, M., 2005: Ensemble-derived stationary and flow-dependent background-error covariances: Evaluation in a quasi-operational NWP setting. *Quart. J. Roy. Meteor. Soc.*, **131**, 1013–1043, doi:10.1256/qj.04.15.

——, and M. Charron, 2007: Spectral and spatial localization of background-error correlations for data assimilation. *Quart. J. Roy. Meteor. Soc.*, **133**, 615–630, doi:10.1002/qj.50.

——, P. L. Houtekamer, C. Charette, H. L. Mitchell, and B. He, 2010a: Intercomparison of variational data assimilation and the ensemble Kalman filter for global deterministic NWP. Part I: Description and single-observation experiments. *Mon. Wea. Rev.*, **138**, 1550–1566, doi:10.1175/2009MWR3157.1.

——, ——, ——, ——, and ——, 2010b: Intercomparison of variational data assimilation and the ensemble Kalman filter for global deterministic NWP. Part II: One-month experiments with real observations. *Mon. Wea. Rev.*, **138**, 1567–1586, doi:10.1175/2009MWR3158.1.

Chang, C.-C., S.-C. Yang, and C. Keppenne, 2014: Applications of the mean recentering scheme to improve typhoon track prediction: A case study of Typhoon Nanmadol (2011). *J. Meteor. Soc. Japan*, **92**, 559–584, doi:10.2151/jmsj.2014-604.

Clayton, A. M., A. C. Lorenc, and D. M. Barker, 2013: Operational implementation of a hybrid ensemble/4D-Var global data assimilation system at the Met Office. *Quart. J. Roy. Meteor. Soc.*, **139**, 1445–1461, doi:10.1002/qj.2054.

Courtier, P., J. N. Thépaut, and A. Hollingsworth, 1994: A strategy for operational implementation of 4D-Var, using an incremental approach. *Quart. J. Roy. Meteor. Soc.*, **120**, 1367–1387, doi:10.1002/qj.49712051912.

Duc, L., K. Saito, and H. Seko, 2013: Spatial-temporal fractions verification for high-resolution ensemble forecasts. *Tellus*, **65A**, 18171, doi:10.3402/tellusa.v65i0.18171.

Ebert, E. E., 2009: Neighborhood verification: A strategy for rewarding close forecasts. *Wea. Forecasting*, **24**, 1498–1510, doi:10.1175/2009WAF2222251.1.

Elsberry, R., 1995: Tropical cyclone motion. *Global Perspectives on Tropical Cyclones*, WMO/TD-693, WMO, 106–197.

Gaspari, G., and S. E. Cohn, 1999: Construction of correlation functions in two and three dimensions. *Quart. J. Roy. Meteor. Soc.*, **125**, 723–757, doi:10.1002/qj.49712555417.

Gentry, M. S., and G. M. Lackmann, 2010: Sensitivity of simulated tropical cyclone structure and intensity to horizontal resolution. *Mon. Wea. Rev.*, **138**, 688–704, doi:10.1175/2009MWR2976.1.

Hamill, T. M., and C. Snyder, 2000: A hybrid ensemble Kalman filter-3D variational analysis scheme. *Mon. Wea. Rev.*, **128**, 2905–2919, doi:10.1175/1520-0493(2000)128<2905:AHEKFV>2.0.CO;2.

Honda, Y., 2010: Tangent linear and adjoint models (in Japanese). Separate volume of annual report of JMA-NPD, Vol. 56, 25–30.

——, and K. Sawada, 2009: Upgrade of the operational mesoscale 4D-Var system at the Japan Meteorological Agency. CAS/JSC WGNE Research Activities in Atmospheric and Oceanic Modelling 2009, J. Côté, Ed., Rep. 39, 2 pp. [Available online at http://www.wcrp-climate.org/WGNE/BlueBook/2009/individual-articles/01_Honda_Yuki_jnova.pdf.]

——, M. Nishijima, K. Koizumi, Y. Ohta, K. Tamiya, T. Kawabata, and T. Tsuyuki, 2005: A pre-operational variational data assimilation system for a non-hydrostatic model at the Japan Meteorological Agency: Formulation and preliminary results. *Quart. J. Roy. Meteor. Soc.*, **131**, 3465–3475, doi:10.1256/qj.05.132.

Hunt, B., and Coauthors, 2004: Four-dimensional ensemble Kalman filtering. *Tellus*, **56A**, 273–277, doi:10.1111/j.1600-0870.2004.00066.x.

Hunt, B. R., E. J. Kostelich, and I. Szunyogh, 2007: Efficient data assimilation for spatiotemporal chaos: A local ensemble transform Kalman filter. *Physica D*, **230**, 112–126, doi:10.1016/j.physd.2006.11.008.

Ikawa, M., and K. Saito, 1991: Description of a nonhydrostatic model developed at the Forecast Research Department of the MRI. MRI Tech. Rep. 28, doi:10.11483/mritechrepo.28.

Ishida, J., 2007: Development of a hybrid terrain-following vertical coordinate for JMA non-hydrostatic model. CAS/JSC WGNE Research Activities in Atmospheric and Oceanic Modelling 2007, J. Côté, Ed., Rep. 37, WMO/TD 1397, 2 pp. [Available online at http://www.wcrp-climate.org/WGNE/BlueBook/2007/individual-articles/03_Ishida_Junichi_wgne_zhybrid.pdf.]

Ito, K., T. Kuroda, K. Saito, and A. Wada, 2015: Forecasting a large number of tropical cyclone intensities around Japan using a high-resolution atmosphere–ocean coupled model. *Wea. Forecasting*, **30**, 793–808, doi:10.1175/WAF-D-14-00034.1.

JMA, 2013: Outline of the operational numerical weather prediction at the Japan Meteorological Agency. Accessed 19 July 2016. [Available online at http://www.jma.go.jp/jma/jma-eng/jma-center/nwp/outline2013-nwp/index.htm.]

Johnson, C., B. J. Hoskins, and N. K. Nichols, 2005: A singular vector perspective of 4D-Var: Filtering and interpolation. *Quart. J. Roy. Meteor. Soc.*, **131**, 1–19, doi:10.1256/qj.03.231.

Kain, J. S., and J. M. Fritsch, 1990: A one-dimensional entraining/detraining plume model and its application in convective parameterization. *J. Atmos. Sci.*, **47**, 2784–2802, doi:10.1175/1520-0469(1990)047<2784:AODEPM>2.0.CO;2.

Kleist, D. T., and K. Ide, 2015: An OSSE-based evaluation of hybrid variational–ensemble data assimilation for the NCEP GFS. Part I: System description and 3D-Hybrid results. *Mon. Wea. Rev.*, **143**, 433–451, doi:10.1175/MWR-D-13-00351.1.

Kuhl, D. D., T. E. Rosmond, C. H. Bishop, J. McLay, and N. L. Baker, 2013: Comparison of hybrid ensemble/4DVar and 4DVar within the NAVDAS-AR data assimilation framework. *Mon. Wea. Rev.*, **141**, 2740–2758, doi:10.1175/MWR-D-12-00182.1.

Kunii, M., 2014: Mesoscale data assimilation for a local severe rainfall event with the NHM-LETKF system. *Wea. Forecasting*, **29**, 1093–1105, doi:10.1175/WAF-D-13-00032.1.

Liu, D. C., and J. Nocedal, 1989: On the limited memory BFGS method for large scale optimization. *Math. Program.*, **45**, 503–528, doi:10.1007/BF01589116.

Lorenc, A. C., 2003a: Modelling of error covariances by 4D-Var data assimilation. *Quart. J. Roy. Meteor. Soc.*, **129**, 3167–3182, doi:10.1256/qj.02.131.

——, 2003b: The potential of the ensemble Kalman filter for NWP—A comparison with 4D-Var. *Quart. J. Roy. Meteor. Soc.*, **129**, 3183–3203, doi:10.1256/qj.02.132.

Miyoshi, T., and S. Yamane, 2007: Local ensemble transform Kalman filtering with an AGCM at a T159/L48 resolution. *Mon. Wea. Rev.*, **135**, 3841–3861, doi:10.1175/2007MWR1873.1.

Nagata, K., 2011: Quantitative precipitation estimation and quantitative precipitation forecasting by the Japan meteorological agency. RSMC Tokyo–Typhoon Center Tech. Rev., **13**, 37–50. [Available online at http://www.jma.go.jp/jma/jma-eng/jma-center/rsmc-hp-pub-eg/techrev/text13-2.pdf.]

Nakanishi, M., and H. Niino, 2004: An improved Mellor–Yamada level-3 model with condensation physics: Its design and verification. *Bound.-Layer Meteor.*, **112**, 1–31, doi:10.1023/B:BOUN.0000020164.04146.98.

Pan, Y., K. Zhu, M. Xue, X. Wang, M. Hu, S. G. Benjamin, S. S. Weygandt, and J. S. Whitaker, 2014: A GSI-based coupled EnSRF–En3DVar hybrid data assimilation system for the operational rapid refresh model: Tests at a reduced resolution. *Mon. Wea. Rev.*, **142**, 3756–3780, doi:10.1175/MWR-D-13-00242.1.

Parrish, D. F., and J. C. Derber, 1992: The National Meteorological Center's spectral statistical-interpolation analysis system. *Mon. Wea. Rev.*, **120**, 1747–1763, doi:10.1175/1520-0493(1992)120<1747:TNMCSS>2.0.CO;2.

Poterjoy, J., and F. Zhang, 2014: Intercomparison and coupling of ensemble and four-dimensional variational data assimilation methods for the analysis and forecasting of Hurricane Karl (2010). *Mon. Wea. Rev.*, **142**, 3347–3364, doi:10.1175/MWR-D-13-00394.1.

Saito, K., 2012: The JMA Nonhydrostatic model and its applications to operation and research. *Atmospheric Model Applications*, I. Yucel, Ed., InTech, 85–110, doi:10.5772/35368.

——, and Coauthors, 2006: The operational JMA nonhydrostatic mesoscale model. *Mon. Wea. Rev.*, **134**, 1266–1298, doi:10.1175/MWR3120.1.

——, T. Kuroda, M. Kunii, and N. Kohno, 2010: Numerical simulation of Myanmar cyclone Nargis and the associated storm surge. Part II: Ensemble prediction. *J. Meteor. Soc. Japan*, **88**, 547–570, doi:10.2151/jmsj.2010-316.

——, M. Hara, M. Kunii, H. Seko, and M. Yamaguchi, 2011: Comparison of initial perturbation methods for the mesoscale ensemble prediction system of the Meteorological Research Institute for the WWRP Beijing 2008 Olympics Research and Development Project (B08RDP). *Tellus*, **63A**, 445–467, doi:10.1111/j.1600-0870.2010.00509.x.

——, H. Seko, M. Kunii, and T. Miyoshi, 2012: Effect of lateral boundary perturbations on the breeding method and the local ensemble transform Kalman filter for mesoscale ensemble prediction. *Tellus*, **64A**, 11594, doi:10.3402/tellusa.v64i0.11594.

Schwartz, C. S., and Z. Liu, 2014: Convection-permitting forecasts initialized with continuously cycling limited-area 3DVAR, ensemble Kalman filter, and "hybrid" variational–ensemble data assimilation systems. *Mon. Wea. Rev.*, **142**, 716–738, doi:10.1175/MWR-D-13-00100.1.

——, ——, X.-Y. Huang, Y.-H. Kuo, and C.-T. Fong, 2013: Comparing limited-area 3DVAR and hybrid variational-ensemble data assimilation methods for typhoon track forecasts: Sensitivity to outer loops and vortex relocation. *Mon. Wea. Rev.*, **141**, 4350–4372, doi:10.1175/MWR-D-13-00028.1.

Wang, X., C. Snyder, and T. M. Hamill, 2007: On the theoretical equivalence of differently proposed ensemble–3DVAR hybrid analysis schemes. *Mon. Wea. Rev.*, **135**, 222–227, doi:10.1175/MWR3282.1.

Wilks, D. S., 2011: *Statistical Methods in the Atmospheric Sciences*. 3rd ed. International Geophysics Series, Vol. 100, Academic Press, 704 pp.

Wu, C.-C., J.-H. Chen, P.-H. Lin, and K.-H. Chou, 2007: Targeted observations of tropical cyclone movement based on the adjoint-derived sensitivity steering vector. *J. Atmos. Sci.*, **64**, 2611–2626, doi:10.1175/JAS3974.1.

Yokota, S., K. Masaru, A. Kazumasa, and O. Seiji, 2016: Comparison between four-dimensional LETKF and ensemble-based variational data assimilation with observation localization. *SOLA*, **12**, 80–85, doi:10.2151/sola.2016-019.

Zhang, M., and F. Zhang, 2012: E4DVar: Coupling an ensemble Kalman filter with four-dimensional variational data assimilation in a limited-area weather prediction model. *Mon. Wea. Rev.*, **140**, 587–600, doi:10.1175/MWR-D-11-00023.1.